

Modeling the impact of neurovascular coupling impairments on BOLD-based functional connectivity at rest



Mario E. Archila-Meléndez, MD, PhD^{a,b}, Christian Sorg, MD^{a,b}, Christine Preibisch, PhD^{a,b,c,*}

^a Technical University of Munich, School of Medicine, Klinikum Rechts der Isar, Department of Diagnostic and Interventional Neuroradiology, Ismaningerstr. 22, 81675, Munich, Germany

^b Technical University of Munich, School of Medicine, Klinikum Rechts der Isar, TUM Neuroimaging Center, Ismaningerstr. 22, 81675, Munich, Germany

^c Technical University of Munich, School of Medicine, Klinikum Rechts der Isar, Clinic for Neurology, Ismaningerstr. 22, 81675, Munich, Germany

ARTICLE INFO

ABSTRACT

Keywords:

Dynamic BOLD simulations
Hemodynamic-metabolic impairments
BOLD-Functional connectivity
BOLD fluctuations

Functional magnetic resonance imaging (fMRI) of blood oxygenation level dependent (BOLD) signals during the resting-state is widely used to study functional connectivity (FC) of slowly fluctuating ongoing brain activity (BOLD-FC) in humans with and without brain diseases. While physiological impairments, e.g. aberrant perfusion or vascular reactivity, are common in neurological and psychiatric disorders, their impact on BOLD-FC is widely unknown and ignored. The aim of our simulation study, therefore, was to investigate the influence of impaired neurovascular coupling on resting-state BOLD-FC.

Simulated BOLD signals comprising intra- and extravascular contributions were derived from an adjusted balloon model, which allows for independent definitions of cerebral blood flow (CBF) and cerebral metabolic rate of oxygen (CMRO₂) responses, being elicited by a synthetic oscillatory input signal with low frequency (0.05 Hz) amplitude modulations. BOLD-FC was then defined by correlations between physiological reference BOLD time curves (seeds of seed-based BOLD-FC) and the test BOLD time curves (targets of BOLD-FC) featuring altered physiological variables (CMRO₂, CBF, cerebral blood volume (CBV)). Impact of impaired neurovascular coupling on BOLD-FC was investigated for three different scenarios with independent changes in (1) CBF and CMRO₂ amplitudes, (2) CBF and CMRO₂ delays, and (3) coupling between CBF and CBV.

For scenario 1, we found 'linear' influences of CMRO₂ and CBF amplitudes on BOLD-FC: for a given CMRO₂ amplitude, BOLD-FC changes from negative to positive FC with increasing CBF amplitude, and increasing CMRO₂ amplitude simply shifts this dependence linearly. For scenario 2, CMRO₂ and CBF delays had a complex 'non-linear' effect on BOLD-FC: for small CMRO₂ delays, we found that BOLD-FC changes from positive to negative BOLD-FC with increasing CBF delays, but for large CMRO₂ delays positive BOLD-FC simply diminishes with increasing CBF delay. For scenario 3, changes in CBF-CBV coupling have almost no effect on BOLD-FC. All these changes were not critically influenced by both signal-to-noise-ratio and temporal resolution modulations.

Our results demonstrate the importance of alterations in neurovascular coupling for aberrant resting-state BOLD-FC. Based on our data, we suggest to complement BOLD-FC studies, at least of at-risk patient populations, with perfusion and oxygenation sensitive MRI. In cases where this is not available, we recommend careful interpretation of BOLD-FC results considering previous findings about hemodynamic-metabolic changes. In the future, accurate modeling of the hemodynamic-metabolic context might improve both our understanding of the crucial interplay between vascular-hemodynamic-neuronal components of intrinsic BOLD-FC and the evaluation of aberrant BOLD-FC in brain diseases with vascular-hemodynamic impairments.

1. Introduction

Blood oxygenation level dependent (BOLD) functional magnetic

resonance imaging (fMRI) (Kwong et al., 1992; Ogawa et al., 1992) at the resting-state (rs-fMRI) (Biswal et al., 1995) is widely used to study human brain functional connectivity (FC) of slowly fluctuating ongoing activity (BOLD-FC or briefly FC) (Fox and Raichle, 2007). In patients with brain

* Corresponding author. Technical University of Munich, School of Medicine, Klinikum rechts der Isar, Department of Diagnostic and Interventional Neuroradiology, Ismaninger Straße 22, 81675, München, Germany.

E-mail addresses: mario.archila@tum.de (M.E. Archila-Meléndez), christian.sorg@tum.de (C. Sorg), preibisch@tum.de (C. Preibisch).

Abbreviations

BOLD	blood oxygenation level dependent
BOLD-FC	rs-fMRI-based measure of functional connectivity
BOLD-TC	BOLD signal time curve
CBF	cerebral blood flow
CBV	cerebral blood volume
CMRO ₂	cerebral metabolic rate of oxygen
CVR	cerebro-vascular reactivity
FC	functional connectivity
fMRI	functional magnetic resonance imaging
MRI	magnetic resonance imaging
rs-fMRI	resting state fMRI

diseases, alterations in BOLD-FC are commonly interpreted in terms of neuronal impairments (Greicius et al., 2004; Sorg et al., 2007; Zhang and Raichle, 2010; Manoliu et al., 2014; Avram et al., 2018; Brandl et al., 2019). BOLD signals, however, result from a complex interplay of neuronal and hemodynamic-metabolic processes, i.e. neurovascular coupling (Bandettini, 2014), implying that the validity of inferring neuronal impairments from altered BOLD-FC requires a tight coupling between neuronal activity and subsequent hemodynamic processes (see Fig. 1). This ambiguity of BOLD signals, substantially hinders full understanding and use of aberrant BOLD-FC in both clinical neuroscience and its application.

The importance of neurovascular coupling for BOLD fMRI has been recognized from its very beginning (Ogawa et al., 1993). Models have been developed, on the one hand, to calibrate task-related BOLD

responses with the aim to achieve a better comparability of task-related neuronal responses (Davis et al., 1998; Chiarelli et al., 2007; Hoge, 2012; Blockley et al., 2013), and on the other hand, to understand and describe transient dynamic features of the BOLD response (Buxton et al., 1998; Obata et al., 2004; Simon and Buxton, 2015). Currently, awareness with respect to the influence of physiological factors on the BOLD signal is increasing – also with respect to resting-state fMRI (Chang et al., 2008; Lv et al., 2013; Liang et al., 2013; Liu, 2013; Tak et al., 2014; Christen et al., 2015; Golestan et al., 2016; Kielar et al., 2016; Liu et al., 2017; Lecrux et al., 2019). Recently, the importance of modeling BOLD signal transients (Havlicek et al., 2017) and significant impact of healthy hemodynamic response function variability on BOLD-FC has been demonstrated (Rangaprakash et al., 2018). Considering rs-fMRI as kind of a ‘spontaneous event-related’ design, Wu et al. developed a deconvolution technique (Wu et al., 2013) that has been proposed to be able to track changes in neurovascular coupling, because it principally allows to extract modulated spontaneous hemodynamic responses from rs-fMRI (Wu et al., 2019).

More pronounced hemodynamic changes, e.g. hypo-perfusion and reduced cerebrovascular reactivity, are known to occur in neurological (Liu et al., 2017; Richter et al., 2017; De Vis, Bhogal et al., 2018; Göttler et al., 2019; Pelizzari et al., 2019; Stickland et al., 2019) as well as psychiatric disorders (Fleisher et al., 2009; Alexopoulos et al., 2012; Peca et al., 2013; Chen, 2018; Oliveira et al., 2018; Riederer et al., 2018; Göttler et al., 2019), and even healthy aging (Ances et al., 2009; Preibisch et al., 2011; De Vis, Hendrikse et al., 2015; West et al., 2019). More specifically, these studies document alterations in oxygen metabolism, i.e. cerebral metabolic rate of oxygen (CMRO₂), as well as perfusion, i.e. cerebral blood flow (CBF), cerebral blood volume (CBV) and cerebro-vascular reactivity (CVR), that can be expected to manifest as changes in CMRO₂, CBF and CBV response amplitudes and delays. While the impact

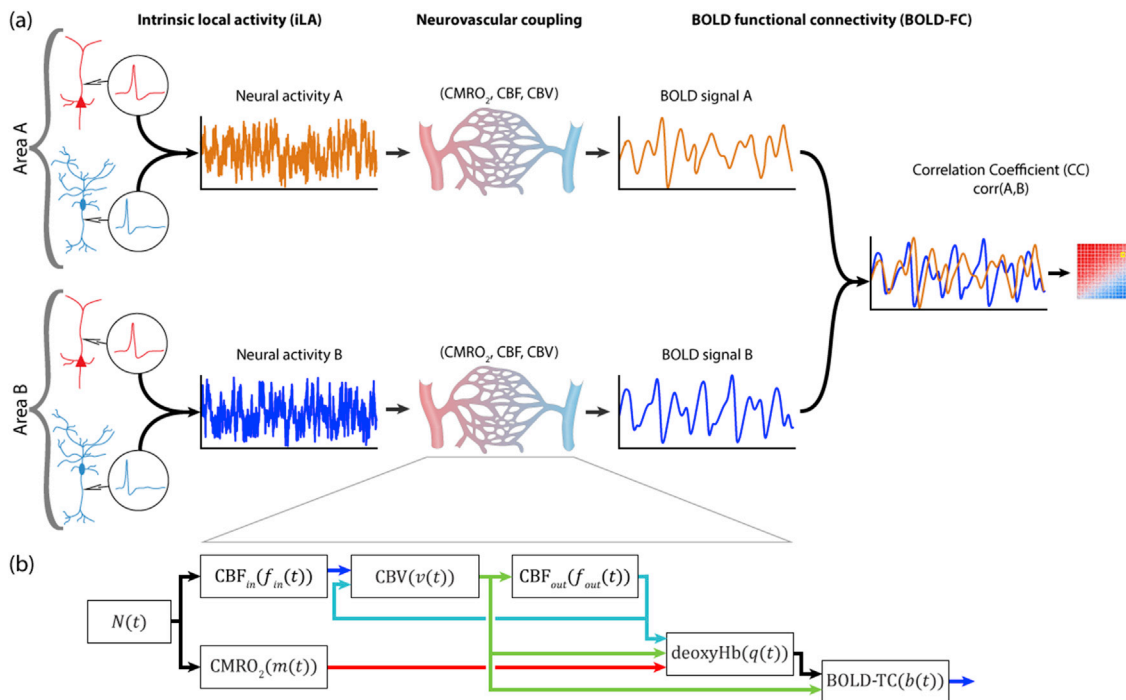


Fig. 1. From intrinsic local activity (iLA) to blood oxygenation level dependent functional connectivity (BOLD-FC) of slowly fluctuating ongoing activity. (a) Neural activity is commonly understood to arise from electrical transmembrane processes emerging from cellular processes (left). Physiological processes, commonly referred to as neurovascular coupling (middle), lead to increases in metabolism (i.e., cerebral rate of oxygen metabolism CMRO₂) and perfusion (i.e., cerebral blood flow (CBF) and volume (CBV)) (Bandettini, 2014). Finally, changes in blood oxygenation level dependent (BOLD) signal can be detected via T2*-weighted magnetic resonance imaging (MRI) (Kwong et al., 1992; Ogawa et al., 1992) (middle-right). Correlations between BOLD signals (Biswal et al., 1995) are interpreted in terms of intrinsic functional connectivity (Fox and Raichle, 2007). The outcome of the investigated dependence of BOLD-FC on neurovascular coupling is symbolized by a schematic BOLD-FC matrix (rightmost red and blue square), whose meaning is explained in Fig. 2. (b) Flow diagram of dynamic BOLD signal simulations accounting for neurovascular coupling.

of reduced CVR (Liu et al., 2017) and arterial delays (Christen et al., 2015; Lv et al., 2013; Chang et al., 2008) on BOLD-FC has impressively been demonstrated, the effects of altered CMRO₂, CBF and CBV have not been systematically investigated yet – neither empirically via multi-modal imaging nor theoretically via simulation approaches.

In this simulation study, we therefore aimed to investigate the influence of hemodynamic and metabolic impairments on the measured BOLD signal, and particularly on BOLD-based FC at rest. We investigated three different hemodynamic-metabolic scenarios by allowing for independent changes in (1) CBF and CMRO₂ amplitudes, (2) CBF and CMRO₂ delays, and (3) CBF-CBV coupling (see Fig. 2). Paradigms for these scenarios are found in neurodegenerative (Iadecola, 2004; Fleisher et al., 2009; Alexopoulos et al., 2012; Peca et al., 2013; Riederer et al., 2018; Göttler et al., 2019) or vascular diseases (Derdeyn et al., 2002; Blicher et al., 2012; Bouvier et al., 2015; De Vis, Petersen et al., 2015; Gersing et al., 2015; Richter et al., 2017; De Vis, Bhogal et al., 2018; Kaczmarz et al., 2018; Göttler et al., 2019), where scenario 1 of altered CMRO₂ and CBF amplitudes corresponds to conditions with exhausted metabolic and vascular reserve capacities, scenario 2 of altered CMRO₂ and CBF delays represents brain tissues where CBF and/or CMRO₂ responses are delayed, and finally scenario 3 of altered CBF-CBV coupling, i.e. altered amplitudes and delays, stands for conditions with exhausted vascular reserve capacity and delayed perfusion. Parameter spaces corresponding to these three conditions were explored for *tight coupling* between CBF and CBV (i.e., *fast CBV responses*) as well as *slower CBV response*. In addition, influences of signal-to-noise-ratio (SNR) and temporal resolution for sampling the BOLD signal were analyzed.

2. Materials and methods

Overview: In order to investigate the impact of impaired hemodynamics and oxygen metabolism on BOLD-FC, we calculated Pearson's correlations between 'non-impaired' reference BOLD time curves (BOLD-TC), serving as seeds S of seed-based FC, and ranges of BOLD-TCs, serving as targets X_{i,j} of FC, representing a wide range of hemodynamic and metabolic alterations. As a surrogate of intrinsic or ongoing slowly fluctuating neuronal activity, we generated a synthetic neuronal input activity N(t) with low frequency amplitude modulations. A dynamic BOLD model allowing for independent CBF and CMRO₂ inputs, was then employed to simulate BOLD signal changes elicited by the neuronal input activity N(t). Even though low frequency BOLD signal fluctuations due to intrinsic ongoing brain activity are strictly not considered as 'BOLD response', which actually is a term from the realm of task-fMRI, we use this term in the following to indicate that the simulated BOLD signal

Table 1

Summary of dynamic model parameters following (Buxton et al., 2004; Simon and Buxton, 2015; Blockley et al., 2009). Default settings employed for simulation of the 'tight coupling' and 'slower CBV' reference curves are accentuated by bold print.

Parameter	Description	Value
N(t)	input intrinsic neuronal activity at time t	dynamic [0–1]
m(t)	ratio of CMRO ₂ at time t to baseline	dynamic
m ₁	CMRO ₂ 'response' amplitude	1.25 [1.0–1.3]
f _{in(t)}	ratio of CBF inflow at time t to baseline	dynamic
f ₁	CBF 'response' amplitude	1.5 [1.0–1.6]
f _{out(t)}	ratio of CBF outflow at time t to baseline	dynamic
q(t)	ratio of deoxyhemoglobin content at time t to baseline	dynamic
v(t)	ratio of venous CBV at time t to baseline	dynamic
h _{f,m} (t)	convolution kernel relating CBF and CMRO ₂ to neuronal input	variable
H _{f,m}	scaling parameter for CBF and CMRO ₂ convolution kernels	variable
τ _{f,m}	characteristic time constants for CBF and CMRO ₂ responses	2s [0.5s–8.0s]
α _v	exponent describing steady state venous flow–volume coupling	0.2 [0.025–0.4]
τ _v	characteristic time constants for venous CBV response	0s (tight coupling), 20s (slower CBV), [0.0s–30.0s]
ν ₀	frequency offset of a fully deoxygenated blood vessel at 3 T	80.6 s ⁻¹ (at 3T)
r ₀	slope defining the dependence of the R2* on blood oxygenation	178 sec ⁻¹ (at 3.0T)
ε	intrinsic ratio of blood to tissue signals at rest	0.24 (at 3.0T)
τ ₀	transit time for blood through venous compartment	0.75s
z	shape parameter for CBF and CMRO ₂ convolution kernels	3
ψ	BOLD-deoxyhemoglobin scaling constant for extravascular BOLD signal contributions (only used in supplement)	≈ 3

fluctuations are in fact elicited by the prescribed neuronal input activity. All described calculations and simulations were implemented and performed using MATLAB R2019b (The MathWorks, Inc.).

Fig. 1 schematically illustrates the assumed relations between the underlying neuronal activities (i.e., neuronal input activity N(t)), induced BOLD responses, and derived BOLD-FC (Fig. 1a) as well as the corresponding simulation framework for modeling their relations (Fig. 1b). Table 1 provides a summary of model parameters as well as their definitions and employed ranges. Fig. 2 illustrates the framework

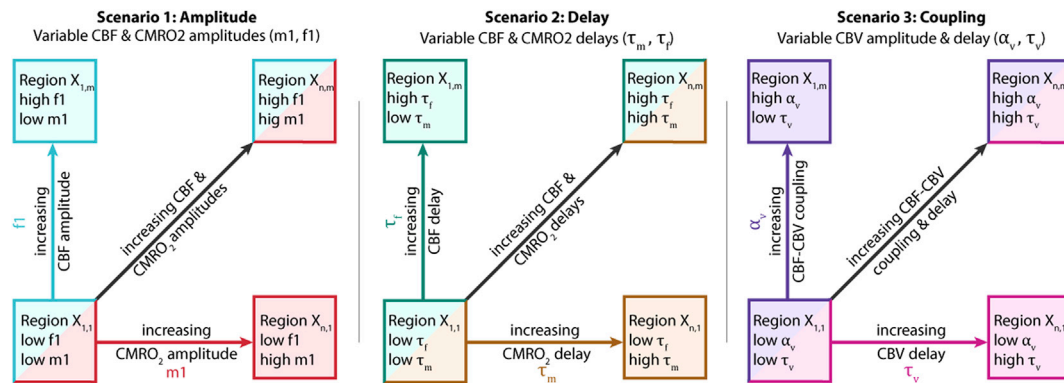


Fig. 2. Framework for exploring the influence of neurovascular coupling on BOLD-FC. The dependence of BOLD-FC on impaired hemodynamic-metabolic coupling processes was investigated by a seed-based FC approach. Specific impairments in the target regions of seed-based FC were systematically simulated across three distinct parameter spaces, i.e. scenarios (left, middle, right), with each scenario spanning a two dimensional space such as varying CMRO₂ amplitude and CBF amplitude in scenario 1 at the left side. These 2-dimensional scenario matrices then allow to visualize the dependence of seed-based BOLD-FC on hemodynamic and metabolic parameters by complementary FC matrices for a fixed seed (see Fig. 1a far right, or Fig. 3). Note that the color scheme for simulated parameters is harmonized with Figs. 3 and 4b, g.

for studying the influence of neurovascular coupling on BOLD-FC in terms of BOLD-FC matrices resulting for the three concrete neurovascular coupling scenarios we investigated. The workflow from influencing parameters across simulated BOLD-TCs to resulting BOLD-FC matrices is summarized in Fig. 3. To reflect BOLD-FC, Pearson's correlation coefficients were calculated between 'non-impaired' reference BOLD signals (seed regions S) and a range of 'impaired' BOLD signal time curves (BOLD-TCs; target regions $X_{i,j}$).

2.1. Simulating the influence of hemodynamic-metabolic impairments on BOLD-FC for three paradigmatic scenarios

Three different paradigmatic scenarios were explored:

- (1) *Scenario 1 – CMRO₂ and CBF amplitudes*: Independent changes in CMRO₂ and CBF response amplitudes (m_1, f_1) were simulated to explore the effects of a quantitative uncoupling between oxygen consumption and blood flow responses (Fig. 2, left). This includes the extremes of maximum CBF response ($f_1 = 1.6$, i.e. 60% CBF increase) at missing CMRO₂ response ($m_1 = 1.0$, i.e. no CMRO₂ increase) as well as missing CBF response ($f_1 = 1.0$, i.e. no CBF increase) at maximum CMRO₂ response ($m_1 = 1.3$ i.e. 30% CMRO₂ increase). These extremes are meant to represent brain tissues that are unable to adapt either oxygen metabolism or perfusion to increased metabolic demands, with otherwise preserved function, i.e. perfusion or metabolism. This corresponds to scenarios where either metabolic or vascular reserve capacities are exhausted, which might be the case in either neurodegenerative (Iadecola, 2004; Fleisher et al., 2009; Alexopoulos et al., 2012; Peca et al., 2013; Riederer et al., 2018; Göttler et al., 2019) or vascular diseases (Derdeyn et al., 2002; Bouvier et al., 2015; De Vis, Petersen et al., 2015; Gersing et al., 2015; Cogswell et al., 2017; De Vis, Bhogal et al., 2018; Göttler et al., 2019).
- (2) *Scenario 2 – CMRO₂ and CBF delays*: Independent changes in CMRO₂ and CBF delays, i.e. the respective characteristic time constants (τ_m, τ_f), were simulated to explore the effects of a temporal uncoupling between oxygen consumption and flow responses (Fig. 2, middle). This comprises the extremes of

immediate CBF response ($\tau_f = 0.5\text{s}$) at delayed CMRO₂ response ($\tau_m = 8.0\text{s}$) as well as delayed CBF response ($\tau_f = 8.0\text{s}$) at prompt CMRO₂ response ($\tau_m = 0.5\text{s}$). Note that τ_m and τ_f influence the time to peak (TTP = $2 \cdot \tau_{m,f}$) as well as the temporal width of the responses (full width at half maximum, FWHM = $3.4 \cdot \tau_{m,f}$). This scenario might represent brain tissues where CBF and/or CMRO₂ responses are delayed, which is present in neurodegenerative or vascular diseases (Fleisher et al., 2009; Iadecola, 2004; Kawano et al., 2016; Khalil et al., 2017; Richter et al., 2017; De Vis, Bhogal et al., 2018; Kaczmarz et al., 2018).

- (3) *Scenario 3 – CBF-CBV coupling*: Independent changes in flow-volume coupling exponent (α_v) and characteristic time constant (τ_v) were simulated to explore effects of independent changes in CBV response amplitudes and delays (Fig. 2, right). This scenario comprises the extremes of instant CBV response ($\tau_v = 0.0\text{s}$) at negligible CBV response amplitude ($\alpha_v = 0.025$) as well as delayed CBV responses ($\tau_v = 30.0\text{s}$) at maximum CBV response amplitude ($\alpha_v = 0.4$). The upper limit for α_v is close to the initially proposed value of 0.38 (Grubb et al., 1974), while more recent estimates yielded rather lower values (Chen and Pike, 2010; Wesolowski et al., 2019). With respect to brain diseases, negligible CBV responses might occur in brain tissues with exhausted vascular reserve capacity, long delays might be present in areas with delayed perfusion due to vessel occlusions (De Vis, Petersen et al., 2015; Kawano et al., 2016; Cogswell et al., 2017; Richter et al., 2017; De Vis, Bhogal et al., 2018; Kaczmarz et al., 2018).

Since the timing of the venous CBV response is controversial – such timing is both difficult to observe and potentially variable across regions, contexts and stimulation conditions (Kim and Kim, 2011; Liu et al., 2019; Hillman et al., 2007; Drew et al., 2011; Hirano et al., 2011; Simon and Buxton, 2015; Lewis et al., 2016; He et al., 2018; Kim et al., 2019), each of the three scenarios was simulated for two characteristic cases of (1) a tight coupling between CBF and CBV, i.e. fast CBV response with $\tau_v = 0.0\text{s}$, and (2) a more loose coupling between CBF and CBV, i.e. slower CBV response with $\tau_v = 20.0\text{s}$ (see Figs. 3 and 4).

For simulations of the physiological reference BOLD time courses, i.e. seeds of BOLD-FC, the prescribed changes in CMRO₂ and CBF amplitudes

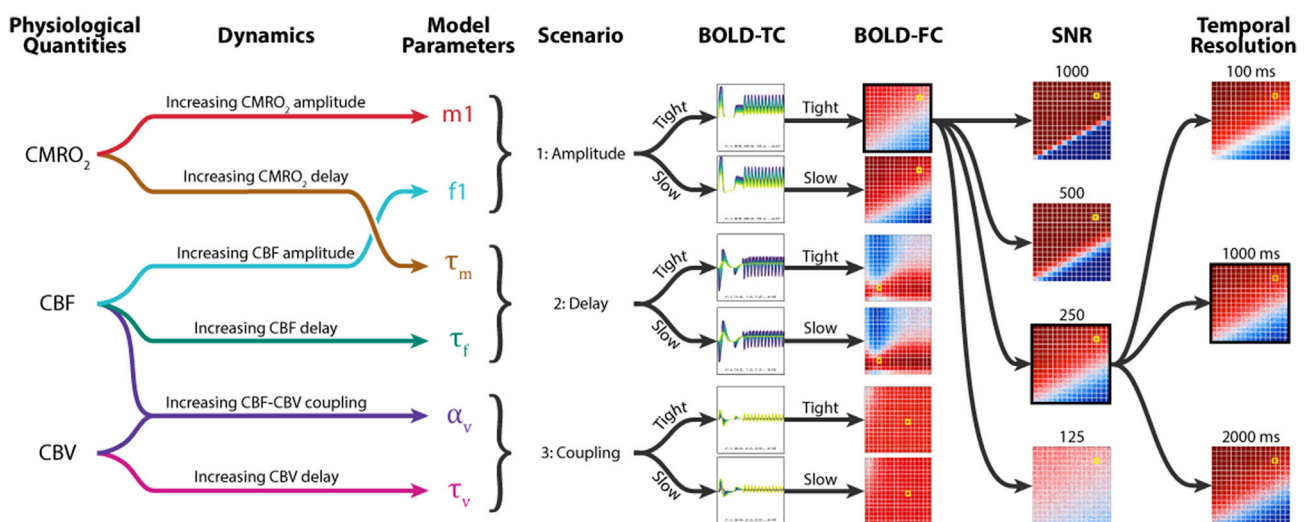


Fig. 3. Overview on simulation scenarios, workflow and results. Temporal changes in CMRO₂, CBF and CBV are simulated using a dynamic BOLD model as illustrated in Fig. 1b. The behavior of normalized CMRO₂ ($m(t)$), CBF ($f(t)$) and CBV ($v(t)$) is governed by prescribed values of CMRO₂ and CBF response amplitudes (m_1, f_1) and characteristic time constants (τ_m, τ_f) as well as CBF-CBV coupling exponent α_v and characteristic time constant τ_v . The flow diagram illustrates, which model parameters are changed in combination (left) to generate BOLD signal time courses (BOLD-TCs) (middle). Correlations between physiological reference BOLD-TCs and impaired target BOLD-TCs (across the parameter spaces of three different scenarios as defined in Fig. 2) results in matrices of correlation coefficients representing BOLD-FC (right). Within those matrices, correlation strength depends on parameter variations (right). To explicitly explore the influence of CBF-CBV coupling, simulations were performed assuming both, tight CBF-CBV coupling ($\tau_v = 0.0\text{s}$) and slower CBV response ($\tau_v = 20.0\text{s}$). Moreover, the influence of SNR and temporal resolution was investigated (far right).

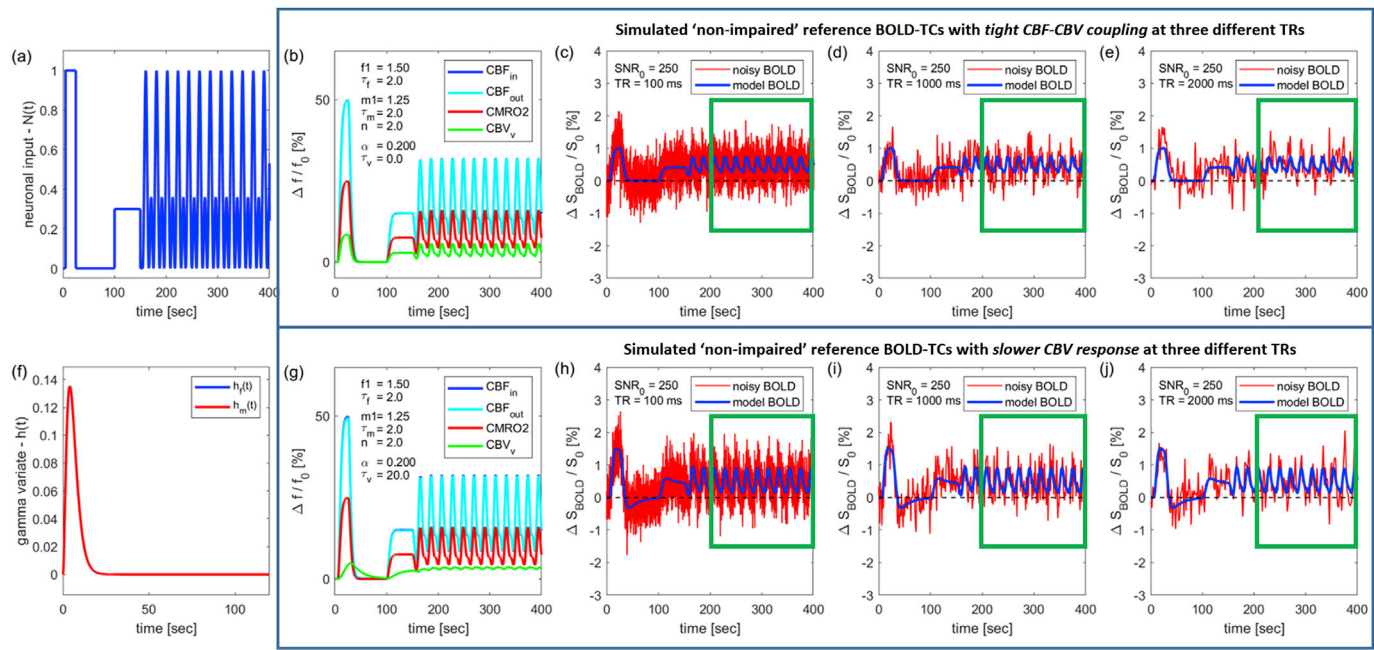


Fig. 4. Seed BOLD time courses - illustration of the simulation process (left) and summary of all BOLD reference signals (right). **Left (a,f):** Convolution of the neuronal input signal $N(t)$ (a) with gamma variate functions $h_f(t)$ and $h_m(t)$ (note that both functions are overlapping) (f) yields independent normalized inputs $f_{in}(t)$ (CBF_{in}) and $m(t)$ (CMRO₂) (b, g). These independent normalized CBF and CMRO₂ inputs, CBF_{in}(t) and CMRO₂(t), were simulated assuming either a tight coupling between CBF and CBV ($\tau_v = 0.0$ s) (b) or a slower CBV response ($\tau_v = 20.0$ s) (g). All other parameters were chosen identical. Input CBF_{in} and CMRO₂ are shown together with simulated outflow (CBF_{out} \approx CBF_{in}) and venous CBV (CBV_v) for tight coupling (b) and slower CBV (g). **Right:** The resulting BOLD signals (blue, c-e, h-j) with temporal resolutions of TR = 100 ms (c, h), TR = 1000 ms (d, i) and TR = 2000 ms (e, j) are likewise shown for tight coupling (c-e) and slower CBV (h-j). The resulting BOLD signals (blue, c-e, h-j) are complemented with random white noise yielding noisy BOLD signals (red, c-e, h-j) with SNR₀ = 250. The signal portion used for BOLD-FC calculations are marked by green frames.

($m_1 = 1.25$, $f_1 = 1.5$) as well as characteristic time constants ($\tau_m = 2.0$ s, $\tau_f = 2.0$ s) were chosen according to previous observations and simulations of task responses to rapidly varying stimuli (Simon and Buxton, 2015), which appears plausible for healthy subject's hemodynamic responses to intrinsic neuronal activity. With respect to CBF-CBV coupling, we used $\alpha_v = 0.2$, similar to $\alpha_v = 0.18 \pm 0.02$ (Chen and Pike, 2010) that is commonly accepted for calibrated fMRI applications (Blockley et al., 2013). With respect to the characteristic time constant τ_v , the choices of tight CBF-CBV coupling, i.e. $\tau_v = 0.0$ s, and slower CBV response, i.e. $\tau_v = 20.0$ s, were matched to the respective simulation scenarios. Fig. 4 illustrates the simulation process for the physiological reference BOLD signals (i.e., seeds of BOLD-FC) that were generated with different temporal resolutions (repetition times TR = 100 ms, 1000 ms, 2000 ms) and assuming either tight coupling between CBF and CBV (Fig. 4b–e) or a slower CBV response (Fig. 4g–j). Compared to tight coupling, the BOLD-TCs at slower CBV conditions show characteristic transients (i.e., post-stimulus undershoots) in the boxcar portion of the simulated signal that are known from typical task experiments (Buxton et al., 1998).

While the simulation model will be described in more detail below (sections 2.2 and 2.3), Fig. 5 and Supplementary Fig. S1 illustrate the ranges of simulated target BOLD-TCs (i.e., ‘impaired’ targets of BOLD-FC) by providing incomplete summaries for the cases of slower CBV response and tight CBF-CBV coupling, respectively. Note that coupling of a boxcar portion to the synthetic neuronal input activity $N(t)$ was meant to allow for a prompt assessment of simulated BOLD signal behaviors as illustrated in Figs. 4 and 5.

BOLD-FC calculations were performed using the intrinsic signal portions (i.e., the last 200s) only that are framed by green boxes in Figs. 4 and 5 as well as Supplementary Fig. S1 to S4. Note that seed and target signals from Figs. 4 and 5, respectively, were always simulated consistently, adopting either tight coupling or slower CBV response conditions.

Besides temporal resolution as noted above, we also explored the influence of noise at four different SNR levels, namely SNR = [1000, 500,

250, 125]. Finally, for each pair of parameters, BOLD-FC, i.e. correlation coefficient values, were finally calculated for 16x16 different realizations of added random white noise ($\mu = 1$, $\sigma = 1/\text{SNR}$), which were then represented as matrices of CC and p-values for each scenario (Figs. 6–8).

2.2. Neural input signal

Background. Active neuronal populations synchronize in the gamma-frequency band (i.e., 30–100 Hz), for example during bottom-up sensory processing (Brosch et al., 2002; Schoffelen et al., 2005; Bastos et al., 2012), in the alpha-frequency band (i.e., 8–12 Hz), for example to mediate top-down influences on sensory processing by regulating cortical excitability (Jensen and Mazaheri, 2010; Mayer et al., 2016), and in the infra-slow and slow frequency range (<1 Hz), for example reflecting large-scale coordination of remote processes by cross-frequency coherence and/or slowly propagating global cortical waves (Engel et al., 2013; Matsui et al., 2016; Mateo et al., 2017; Mitra et al., 2018). The current study takes these paradigmatic frequency bands to simulate neural input signals.

Definition of $N(t)$. A continuous oscillatory signal was used to simulate such modes of neuronal activity and applied as the neural input to the below described BOLD simulation model. In detail, three different time series $x(t)$ with the generic form shown in equation (1) were calculated with frequencies 60, 10 and 0.05 Hz.

$$x(t) = A_x * \cos(2\pi f_x t + \phi_x) \quad (1)$$

A power-to-power cross-frequency coherence relationship was implemented in which the time series with the lowest frequency (i.e., 0.05 Hz) modulated the amplitude of the remaining time series (i.e., 60 and 10 Hz). The time-frequency representation (TFR) of the simulated neural signal was sampled in 2 Hz steps between 6 and 80 Hz using a Hanning taper with a length of seven times the cycle length and 10 ms step size. From the resulting TFR, average power was calculated,

normalized and zero-padded to extract a single time course $N(t)$. This signal was coupled to a boxcar portion to allow for prompt assessment of simulated BOLD signal behavior as illustrated in Fig. 4a.

2.3. Dynamic BOLD simulations

Calculation of dynamic BOLD signals from the above described synthetic input neuronal activity $N(t)$, was based on the Balloon model that was originally proposed and further developed by Buxton and coworkers (Buxton et al., 1998; Obata et al., 2004). Our implementation using Simulink and MATLAB R2019b closely resembles the one presented by Simon and Buxton, (2015). With respect to nomenclature, we follow this previous work and stick to their conventions in particular with regard to expressing changes in dynamic variables relative to baseline values (see Table 1). In the following, we provide a concise description of the employed model framework, which is also illustrated in Fig. 1b.

Since we strive to simulate the influence of independent alterations in oxygen metabolism and hemodynamic parameters on BOLD-FC, it is important that the respective model inputs can be defined independently. Following previous work (Buxton et al., 1998; Simon and Buxton, 2015), dynamic changes in incoming blood flow, $f_{in}(t)$, and metabolic rate of oxygen, $m(t)$, relative to baseline, were modeled as linear responses to a prescribed neuronal input $N(t)$:

$$f_{in}(t) = N(t) * h_f(t) \quad (2)$$

$$m(t) = N(t) * h_m(t) \quad (3)$$

where the convolution kernels $h_{f,m}(t)$ are scaled gamma distributions,

$$h_{f,m}(t) = H_{f,m} \frac{1}{\tau_{f,m}} \left(\frac{t}{\tau_{f,m}} \right)^{(z-1)} e^{-t/\tau_{f,m}} \quad (4)$$

with shape parameter z , scaling parameters $H_{f,m}$ and characteristic time constants $\tau_{f,m}$, that take distinct parameters values for flow (f) and metabolic (m) input functions, respectively (see Table 1).

Emanating from these changes in blood flow ($f_{in}(t)$) and oxygen metabolism ($m(t)$) (evoked by the prescribed neuronal input $N(t)$), a system of coupled differential equations is used to derive relative changes in deoxyhemoglobin content, $q(t)$, and venous blood volume, $v(t)$, from which BOLD signal changes relative to baseline (b_0) are calculated. Since the extravascular fraction likely accounts for only about 70% of BOLD signal change at 3T (Li and van Zijl, 2020), we follow the approach of (Obata et al., 2004), who derived an expression including extra- and intravascular signal contributions

$$\frac{b(t) - b_0}{b_0} = V_0 [(k_1 + k_2)(1 - q(t)) - (k_2 + k_3)(1 - v(t))] \quad (5)$$

with $k_1 = 4.3\nu_0 V_0 E_0 TE$, $k_2 = \epsilon r_0 E_0 TE$, and $k_3 = \epsilon - 1$. Besides the frequency offset of a fully deoxygenated blood vessel, $\nu_0 = 80.6 \text{ s}^{-1}$ (Simon and Buxton, 2015) and the echo time $TE = 30 \text{ ms}$, Eq. (5) requires knowledge of the intrinsic ratio of blood to tissue signals at rest, $\epsilon = 0.24$, and the slope defining the dependence of the $R2^*$ relaxation rate on blood oxygenation, $r_0 = 178 \text{ sec}^{-1}$ (see Table 1 in (Blockley et al., 2009)). Additionally, we assumed a baseline fractional venous blood volume, $V_0 = 0.025$, and baseline oxygen extraction fraction, $E_0 = 0.4$ (Leenders et al., 1990; Ishii et al., 1996; Ibaraki et al., 2008). Given the uncertainty in ϵ and r_0 , and in order to investigate the influence of neglecting intravascular contributions, we also calculated BOLD signal changes using a purely extravascular BOLD signal model following Simon and Buxton (2015) (see Supplementary material: Eq. (S1) and Fig. S2 to S7).

The differential equations employed to derive dynamic changes in deoxyhemoglobin content ($q(t)$) are based on principles of mass and volume conservation for deoxyhemoglobin and blood, respectively. Assuming a homogeneous venous compartment, dynamic changes in

deoxyhemoglobin content $q(t)$ result from changes in CMRO₂ ($m(t)$), CBF (more precisely the rate of blood flow out of the compartment $f_{out}(t)$), and subsequent expansion of the venous compartment, i.e. venous blood volume CBV_v ($v(t)$):

$$\frac{dq}{dt} = \frac{1}{\tau_0} [m(t) - f_{out}(v) \frac{q(t)}{v(t)}] \quad (6)$$

where τ_0 is the transit time for blood through the venous compartment.

Equation (7) describes the rate of change of cerebral blood volume relative to baseline $v(t)$ and models its dependence on the difference between its current value $v(t)$ and the value it would reach if the system was allowed to reach a steady state at a given inflow $f_{in}(t)$

$$\frac{dv}{dt} = \frac{1}{\tau_v} [f_{in}^{av}(t) - v(t)] \quad (7)$$

where τ_v is the characteristic time constant of the CBV response and α_v is the exponential flow–volume coupling parameter, originally described to be 0.38 by Grubb et al. (Grubb et al., 1974). We assume $\alpha_v = 0.2$ as a standard, similar to a more recent value of $\alpha_v = 0.18$ (Chen and Pike, 2010). Equation (8) models the dependence of the rate change in $v(t)$ on the difference between inflow and outflow

$$\frac{dv}{dt} = \frac{1}{\tau_0} [f_{in}(t) - f_{out}(t, v)] \quad (8)$$

For the missing blood flow out of the system, $f_{out}(v,t)$, we finally employed a relation that assumes viscoelastic effects in the vascular system (Buxton et al., 1998; Simon and Buxton, 2015)

$$f_{out}(t, v) = \left(v(t) + \tau_v \frac{dv}{dt} \right)^{1/\alpha_v} - \tau_0 \frac{dv}{dt} \quad \text{for } \tau_v > 0 \quad (9)$$

$$f_{out}(t, v) = v^{1/\alpha} + \tau_0 \frac{dv}{dt} \quad \text{for } \tau_v = 0 \quad (10)$$

where the vasculature, i.e. the ‘balloon’, initially resists volume changes but then approaches a new steady-state in accordance with a power law dependence between blood flow and volume.

Fig. 4 illustrates the simulation process for the reference BOLD-TCs of seed-based BOLD-FC obtained by convolution of the prescribed neuronal input signal $N(t)$ (Fig. 4a) with independent hemodynamic response functions $h_f(t)$ and $h_m(t)$ (Fig. 4f) for presumably healthy CMRO₂ ($m_1 = 1.25$, $\tau_m = 2.0\text{s}$) and CBF ($f_1 = 1.5$, $\tau_f = 2.0\text{s}$) response parameters (following (Simon and Buxton, 2015)). This process yields independent normalized input cerebral blood flow $f_{in}(t)$ (CBF_{in}) and metabolic rate of oxygen $m(t)$ (CMRO₂) that are independent from flow-volume coupling conditions (blue and red curves in Fig. 4b, g). Simulated changes in venous CBV_v ($v(t)$) (green curves in Fig. 4b, g) and blood flow out of the tissue CBF_{out} ($f_{out}(t)$) (\approx CBF_{in}, cyan curves in Fig. 4b, g) depend on assumed flow-volume coupling conditions. Resulting BOLD-TCs are shown for both (1) tight coupling between CBF and CBV ($\alpha_v = 0.2$, $\tau_v = 0.0\text{s}$) (Fig. 4c-e) and (2) slower CBV response ($\alpha_v = 0.2$, $\tau_v = 20.0\text{s}$) (Fig. 4h-j). Fig. 5 and Supplementary Fig. S1 show incomplete summaries of noise-free simulated BOLD signal time curves for slower CBV response and tight CBF-CBV coupling, respectively. Note that signal correlations for BOLD-FC calculations were only performed on the green-rimmed signal portions (i.e., the last 200s) of simulated BOLD-TCs exhibiting low frequency oscillations, which also excludes transients resulting from the border between constant and oscillating neuronal input signal $N(t)$.

3. Results

Fig. 3 presents an overview of both the workflow and, importantly, the main results of our study – from the investigated parameters (left) over the three simulated scenarios and BOLD-TCs (left-middle) to the results with respect to BOLD-FC (right). The simulated physiological (i.e.,

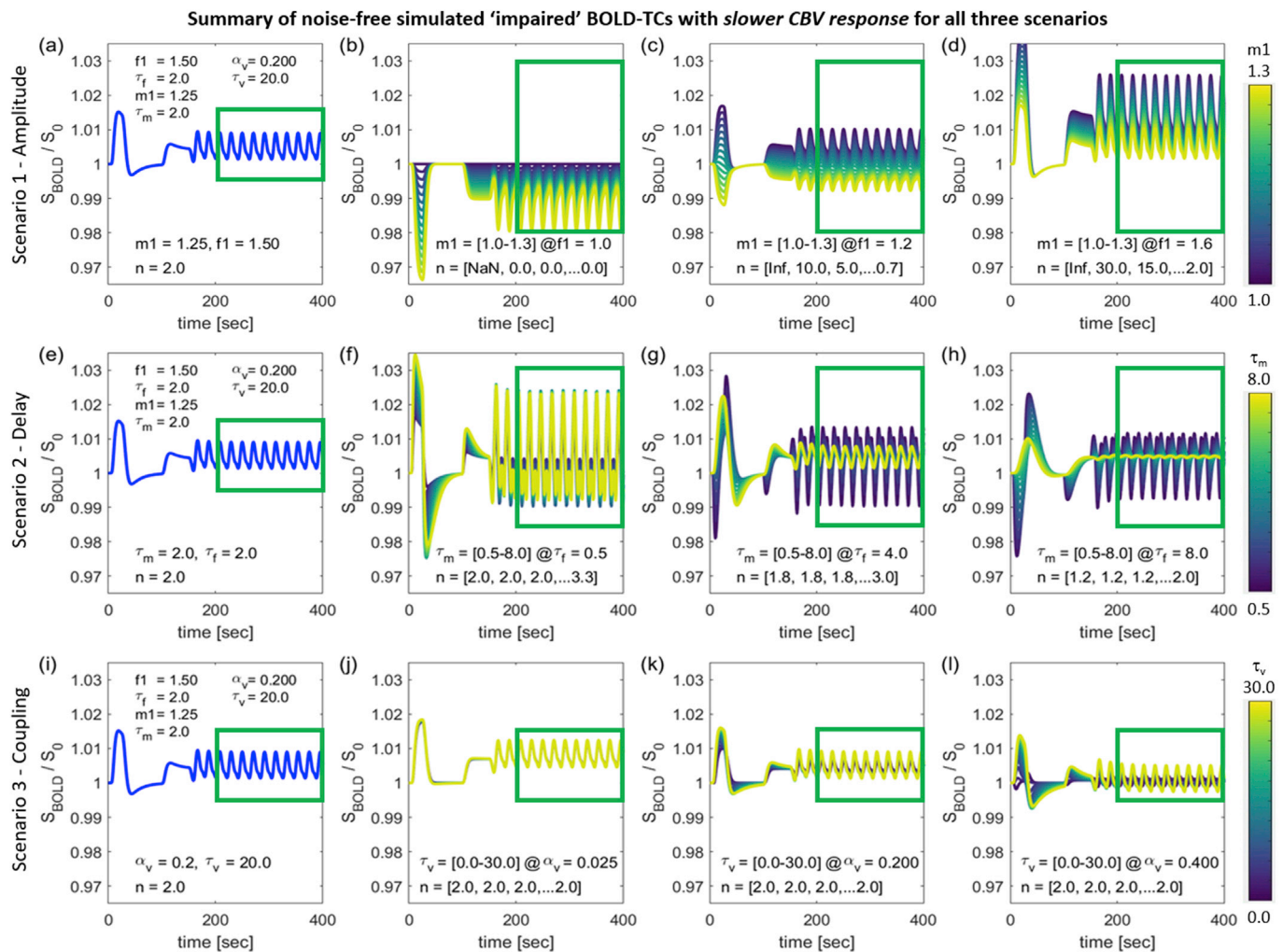


Fig. 5. Summary of simulated noise-free ‘impaired’ target BOLD signal time curves (BOLD-TCs) for all three scenarios at slower CBV response ($\tau_v = 20$ s). **Left:** For comparison, the first column (a, e, i) shows the respective physiological reference BOLD-TC, which is actually identical for all three scenarios and replicates Fig. 4i. **Right:** Target BOLD-TCs of impaired hemodynamic-metabolic physiology. The top row (Scenario 1 – Amplitude, b-d) shows BOLD-TCs resulting from the simulated range of changes in evoked CMRO₂ amplitude (m1) at three different CBF amplitudes (f1). The middle row (Scenario 2 – Delay, f-h) shows BOLD-TCs resulting from the simulated range of delays in oxygen metabolism (τ_m) at three different CBF delays (τ_f). The bottom row (Scenario 3 – Coupling, j-l) shows BOLD signals resulting from the simulated range of delays in CBV responses (τ_v) at three different flow-volume coupling exponents (α_v). For plots with multiple simulated curves, line colors change from dark blue to yellow along the given ranges of m1 (b-d), τ_m (f-h) and τ_v (j-l) as indicated by the color bars. Signal portions used for BOLD-FC calculations are marked by green frames and correspond to the last 200 s.

‘non-impaired’) reference BOLD signal time curves used as seeds of BOLD-FC are shown in Fig. 4c-e (i.e., tight coupling between CBF and CBV) and Fig. 4h-j (i.e., slower CBV) for three different temporal resolutions, TR = 100 ms (Fig. 4c,h), TR = 1000 ms (Fig. 4d,i), TR = 2000 ms (Fig. 4e,j). For the prescribed temporal SNR₀ = 250, the BOLD-TCs appear reasonably realistic. The behavior of the simulated BOLD signals can be best assessed in the initial boxcar portion, where a typical post-stimulus undershoot can be observed for the signals simulated with slower CBV response (Fig. 4h-j) but not for tight CBF-CBV coupling (Fig. 4c-e).

In Fig. 5, referring to BOLD-TCs of physiologically ‘impaired’ target regions of BOLD-FC, an incomplete summary of noise-free simulated BOLD-TCs is given for the case of slower CBF-CBV coupling at TR = 1000 ms, demonstrating a wide variation of BOLD signal amplitudes as well as shapes. Note that the physiological reference time courses in the first column are in fact identical and replicate Fig. 4i. In particular, there are distinct differences between BOLD-TCs across the three different scenarios that will be presented in detail below, together with scenario-specific, distinct FC changes. Summarized in Supplementary Fig. S1, for the case of tight CBF-CBV coupling, simulated BOLD-TCs look

essentially similar. The most salient difference is the missing post-stimulus undershoot in the boxcar portion of the signals, but one should also note the generally lower amplitude of the BOLD signal changes in the slowly oscillating BOLD-TC portions when tight coupling is assumed. This difference appears particularly pronounced in the reference BOLD-TCs (Fig. 5a,e,i vs. Figure S1a,e,i), which induces systematically lower significances in BOLD-FC in the case of tight coupling (Fig. 6a-f) vs. slower CBV (Fig. 6g-l). Differences between BOLD-TCs simulated at different temporal resolutions (i.e., TR = 100 ms, 1000 ms, 2000 ms) are hardly recognizable (data not shown) and are not expected to impact on the results of BOLD-FC calculations directly, because the simulated BOLD-TCs were complemented with noise before they served as target regions X_{i,j} for BOLD-FC-calculations across the three different scenarios (see Fig. 4 for exemplary noisy BOLD-TCs at SNR₀ = 250).

The following sections describe the overall behavior of both simulated BOLD-TCs of target regions of BOLD-FC (Fig. 5) and BOLD-FCs themselves (Fig. 6) across the parameter spaces of the three different scenarios outlined in Fig. 2. The behavior of BOLD-FC, i.e. the correlation coefficients (CC-values) and their significance levels (p-values), is shown

Influence of different neurovascular coupling scenarios on BOLD-FC

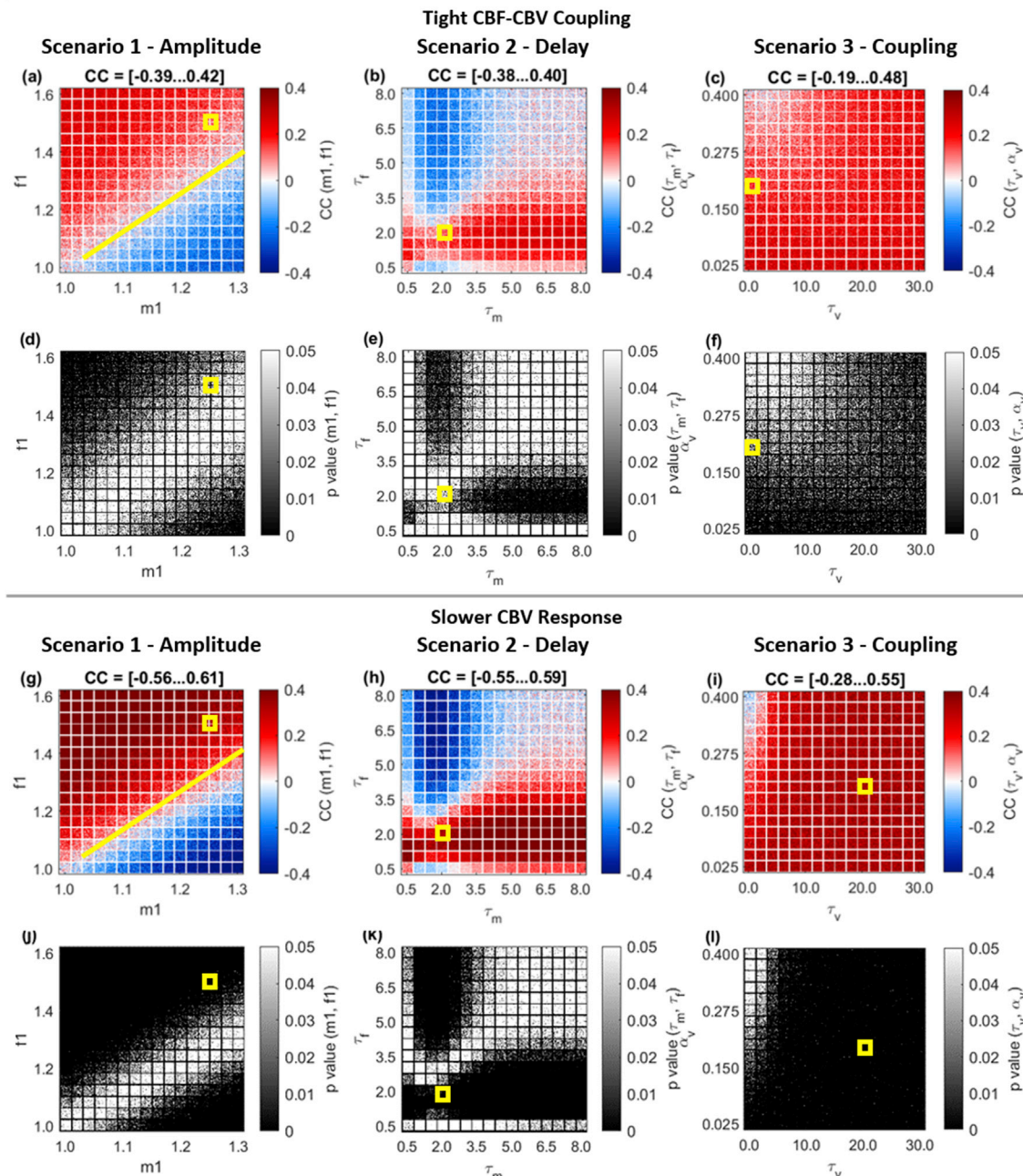


Fig. 6. Influence of different neurovascular coupling scenarios on BOLD-FC. Matrices of correlation coefficients (CC), reflecting seed-based BOLD-FC (a-c, g-i), and corresponding p-values (d-f, j-l) for correlations between ‘non-impaired’ seed BOLD-TCs and ‘impaired’ BOLD-TCs of target regions. Three different parameter spaces (i.e., scenarios) were explored for either tight coupling (a-f) or slower CBV (g-l): scenario 1: amplitude (left), scenario 2: delay (middle), and scenario 3: coupling (right). Results are shown for a temporal resolution of TR 1000 ms and SNR₀ = 250 with 16x16 different random white-noise realizations for each pair of investigated parameter values. The yellow line in panels (a) and (g) indicates where the flow-metabolism coupling ratio n = (f1-1)/(m1-1) ≈ 1.3. The location of the seed reference time curve in the respective parameter spaces is indicated by yellow squares. Matrices of CC values representing BOLD-FC are uniformly scaled between -0.4 and +0.4. For each scenario, the individual range of CC values is noted in the title of each CC matrix. Matrices of p-values are truncated at p = 0.05, rendering voxels with insignificant correlations white.

in Fig. 6 for the assumptions of tight CBF-CBV coupling (Fig. 6a-f) and slower CBV response (Fig. 6g-l). The influence of both different SNR levels (Fig. 7) and temporal resolutions (Fig. 8) on BOLD-FC is then demonstrated for scenario 1 assuming slower CBV responses.

3.1. Scenario 1 – amplitude: influence of CBF and CMRO₂ amplitude changes on BOLD-TCs and BOLD-FC is simple

The overview of main results in Fig. 3 shows that the dependence of

BOLD-FC on CMRO₂ and CBF amplitude is simple: For a given CMRO₂ amplitude, BOLD-FC changes from negative to positive FC with increasing CBF amplitude, and increasing CMRO₂ amplitude simply shifts this dependence linearly. A detailed look (Fig. 6a,g) reveals, that for the case of missing flow response (f1 = 1, along the x-axis), CC-values (i.e. BOLD-FC) become increasingly negative with increasing CMRO₂ amplitude (m1 = [1–1.3]), while for distinct CMRO₂ amplitudes, CC-values go from negative to positive with increasing CBF amplitudes. These areas with negative and positive BOLD-FC are separated by a zone

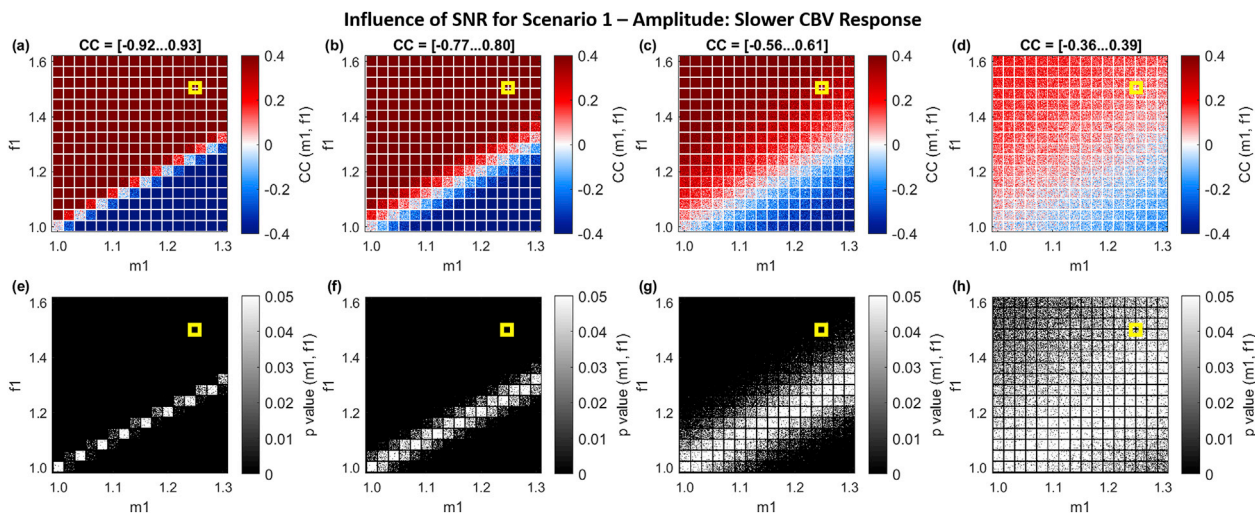


Fig. 7. Influence of different signal-to-noise ratios on BOLD-FC simulations. Correlation coefficients (CC), reflecting BOLD-FC (a-d) and p-values (e-h) for scenario 1: amplitude, assuming slower CBV response. The ‘non-impaired’ physiological reference BOLD-TC and the range of ‘impaired’ target BOLD-TCs were simulated at four different noise levels, SNR = 1000 (a, e), SNR = 500 (b, f), SNR = 250 (= SNR₀) (c, g) and SNR = 125 (d, h), with 16x16 different random white-noise realizations for each pair of investigated parameter values. Note that Fig. 7c,g, corresponding to SNR = 250, duplicates Fig. 6g,j. The location of the seed reference time curve in the parameter space is indicated by a yellow square in each plot. Results are shown for a temporal resolution of TR = 1000 ms. Matrices of CC values representing BOLD-FC are scaled between −0.4 and +0.4. For each scenario, the individual range of CC values [minimum ... maximum] is noted in the title of each CC matrix. Matrices of p-values are truncated at p = 0.05, rendering voxels with insignificant correlations white.

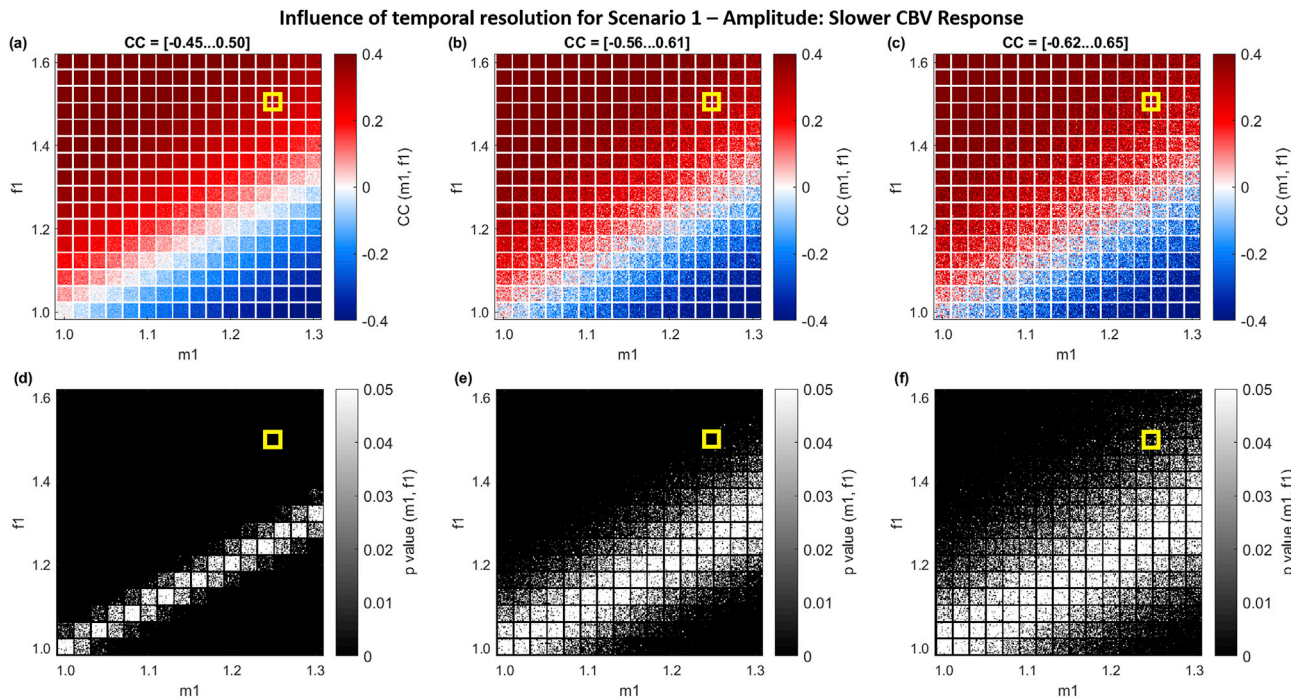


Fig. 8. Influence of temporal resolution on BOLD-FC simulations. Correlation coefficients (CC), reflecting BOLD-FC (a-c) and p-values (d-f) for scenario 1: amplitude, assuming slower CBV response. The ‘non-impaired’ physiological reference BOLD-TC and the range of ‘impaired’ target BOLD-TCs were simulated for three different temporal resolutions, namely at TR = 100 ms (a, d), TR = 1000 ms (b, e) and TR = 2000 ms (c, f). Note that Fig. 8b,e, corresponding to TR = 1000 ms, duplicates Fig. 6g,j. The location of the seed reference time curve in the parameter space is indicated by a yellow square in each plot. Results are shown for SNR₀ = 250 with 16x16 different random white-noise realizations for each pair of investigated parameter values. Matrices of CC values representing BOLD-FC are scaled between −0.4 and +0.4. For each scenario, the individual range of CC values [minimum ... maximum] is noted in the title of each CC matrix. Matrices of p-values are truncated at p = 0.05, rendering voxels with insignificant correlations white.

with CC-values around zero. For tight coupling, this zone extends along a diagonal (marked by a yellow line) where the flow-metabolism coupling ratio $n = (f1-1)/(m1-1) \approx 1.3$, while for slower CBV response, the zone with zero CC values rather extends around $n \approx 1$.

This pattern can easily be understood from the behavior of the BOLD-

TCs (Fig. 5b-d, Supplementary Fig. S1b-d). In the case of missing CBF response ($f1 = 1$, Fig. 5b and S1b), all BOLD signal changes (relative to baseline) are negative, while all signal changes are positive at the maximum CBF amplitude of 60% ($f1 = 1.6$, Fig. 5d and S1b). At an intermediate CBF response of 20% ($f1 = 1.2$), BOLD signal changes vary

from positive to negative with increasing CMRO₂ amplitude ($m_1 = [1-1.3]$, Fig. 5c and S1c). Generally, the target BOLD-TCs with positive or negative BOLD signal changes are perfectly in phase or opposite phase with the reference BOLD-TCs. Accordingly, the correlations of these target BOLD-TCs (Fig. 5b-d and Supplementary Fig. S1b-d) with the reference BOLD-TC (seeds S, Fig. 5a and Supplementary Fig. S1a) are significantly positive or negative in the upper left and lower right corners with maximum CBF and CMRO₂ amplitudes (Fig. 6a,d,g,j), respectively. Between those extreme cases lies a diagonal area, where the fractional increases in CBF hardly surpasses the fractional increases in CMRO₂, i.e. where $n \approx 1.3$ and 1.0 for tight coupling (Fig. 6a) and slower CBV (Fig. 6g), respectively. In this area, BOLD signal changes are negligible in comparison to noise, resulting in non-significant correlations with CC-values around zero. Comparing BOLD-FC behavior simulated for the assumptions of either tight coupling (Fig. 6 a,d) or slower CBV (Fig. 6 g,j), it can be seen that absolute values of correlation coefficients (ranges are noted in the titles) are higher for the slower CBV response and the area with non-significant correlations is also clearly smaller (white diagonal area in Fig. 6j vs. extended areas of non-significant correlations in Fig. 6d). This accords with the generally lower BOLD signal changes observed when assuming tight CBF-CBV coupling as mentioned above (compare Fig. 4c-e vs. 4h-j and Supplementary Fig. S1b-d vs. Fig. 5b-d).

3.2. Scenario 2 – delays: influence of CBF and CMRO₂ delays on BOLD-TCs and BOLD-FC is complex

The overview in Fig. 3 already shows that the dependence of BOLD-FC on CMRO₂ and CBF temporal delays is complex: CBF and CMRO₂ delays exert ‘non-linear’ effects on FC. For small CMRO₂ delays, we found that BOLD-FC changes from positive to negative FC with increasing CBF delays, but for large CMRO₂ delays positive FC simply diminishes with increasing CBF delay. A detailed look (Fig. 6b,h) reveals, that around the reference flow delay ($\tau_f = [1-2]$ s, along the x-axis), CC-values (i.e. BOLD-FC) are positive for all CMRO₂ response delays ($\tau_m = [0.5-8.0]$ s), where the area of positive CC-values shows a marked constriction around the reference CMRO₂ delay ($\tau_m = [1-2]$ s). For low CMRO₂ delays ($\tau_m < 4$ s), CC-values go from positive to negative with increasing CBF delays ($\tau_f > 3$ s). Again, these areas showing positive and negative correlations are separated by transitional areas with CC-values around zero, but here extended areas with negligible correlations exist when both characteristic time constants (τ_m, τ_f) are larger than about 4s.

This complex pattern can be understood from the more complex BOLD signal behaviors that result from variable delays in CMRO₂ and CBF responses, i.e. variations in characteristic time constants (τ_m, τ_f), for tight CBF-CBV coupling (Supplementary Fig. S1e-h) as well as slower CBV response (Fig. 5e-h). In general, marked transients occur, the more CMRO₂ and CBF changes get out of phase with increasing differences between characteristic time constants τ_m and τ_f . Correlations of these target BOLD-TCs (for tight coupling: Supplementary Fig. S1f-h and slower CBV: Fig. 5f-h) with the reference BOLD-TC (i.e., seed S, for tight coupling: Supplementary Fig. S1e and slower CBV: Fig. 5e) are significantly positive in the parameter space centered on $\tau_f = 2$ s and increasing with τ_m . For $\tau_f \approx 4$ s on the other hand, significantly negative correlations are observed, centered on the reference value ($\tau_m = [0.5-4]$ s, (Fig. 6b,e,h,k). In between, getting broader towards the upper right quadrant, exists an extended area with non-significant correlations (i.e., CC-values near zero), where both characteristic time constants τ_m and τ_f are larger than about 4s. According to Supplementary Fig. S1g,h, and Fig. 5g,h, these are areas where BOLD signal changes in the slowly fluctuating intrinsic signal portion converge to zero with increasing τ_m . Comparing BOLD-FC behavior between tight coupling (Fig. 6 b,e) or slower CBV (Fig. 6 h,k), it can be seen that absolute values of correlation coefficients (ranges are noted in the titles) are higher for the slower CBV response (Fig. 6h vs. 6b) and the area with non-significant correlations is also clearly reduced for the case of slower CBV response (Fig. 6k vs. 6e), while differences in BOLD-TCs are less pronounced compared to the

change in the amplitudes scenario 1 (compare Supplementary Fig. S1f-h vs. Fig. 5f-h).

3.3. Scenario 3 – coupling: influence of flow–volume coupling on BOLD-TCs and BOLD-FC is simple and small

The overview in Fig. 3 already indicates that the influence of CBF-CBV coupling on BOLD-FC is relatively minor: Changes in CBF-CBV coupling have almost no effect on FC. A detailed look on Fig. 6c and i reveals that positive correlations prevail with little influence of CBV delay (τ_v) for low flow-volume coupling exponents $\alpha_v < 0.2$. Only for strong CBF-CBV coupling ($\alpha_v > 0.2$) and short characteristic time constants ($\tau_v < 5$ s), CC-values, i.e. BOLD-FC, are markedly reduced.

Again, this can be understood from the behavior of BOLD-TCs. With respect to variations in the flow-volume coupling exponent α_v and the characteristic time constant for the CBV response τ_v , the simulated BOLD-TCs do not vary a lot, especially for low α_v , i.e. weak CBV responses, and high τ_v , i.e. long delays in CBV responses (Fig. 5i-l), while BOLD signal changes converge towards zero for high α_v and low τ_v . With regard to BOLD-FC, this is mirrored by extended areas of significantly positive CC values (Fig. 6c,f,i,l). For slower CBV response (Fig. 6i,l), only a comparably small area with $\alpha_v > 0.2$ and $\tau_v < 5$ shows non-significant correlations (Fig. 6c,i), where negative CC values result from noise because from the BOLD-TCs it is clear that a combination of large α_v (i.e. high CBV response amplitudes) and short τ_v results in negligible BOLD responses. When comparing BOLD-FC behavior between tight coupling (Fig. 6c,f) and slower CBV (Fig. 6i,l), the absolute values of correlation coefficients (ranges are noted in the titles) are clearly higher for the slower CBV response (Fig. 6h vs. 6b) and the area with non-significant correlations is clearly extended for the case of tight coupling (Fig. 6k vs. 6e), while the BOLD-TCs show notable differences in amplitude (compare Supplementary Fig. S1j-l vs. Fig. 5j-l).

3.4. Influence of SNR on BOLD-FC

The influence of temporal SNR on correlation coefficients and corresponding p-values is explored in Fig. 7 for scenario 1, i.e. changes in CBF and CMRO₂ response amplitudes, assuming a slower CBV response. It can be seen that the overall behavior of positive correlations for high CBF amplitudes at rather lower CMRO₂ and negative correlations for high CMRO₂ amplitudes at lower CBF, is preserved throughout (Fig. 7a-d) though absolute CC-values decrease from about 0.93 at SNR = 1000, to about 0.35 at SNR = 125. However, while the areas with significantly positive or negative correlations are separated by only a narrow diagonal area at SNR = 1000, this area with non-significant correlations widens with decreasing SNR (Fig. 7e-g). At SNR = 125 finally, the area of non-significant correlation extends across the whole parameter space (Fig. 7h). Qualitatively similar behavior can be observed for SNR variations for scenarios 2 and 3 (data not shown).

3.5. Influence of temporal resolution on BOLD-FC

The influence of temporal resolution, corresponding to the image sampling repetition time (TR) of BOLD-TCs, on correlation coefficients and corresponding p-values is explored in Fig. 8, also for scenario 1, i.e. changes in CBF and CMRO₂ response amplitudes, and assuming a slower CBV response. It can be seen that the overall behavior of positive correlations for high CBF amplitudes at rather lower CMRO₂ and negative correlations for high CMRO₂ amplitudes at lower CBF, is preserved throughout (Fig. 8a-c) and absolute CC-values increase from about 0.47 at TR = 100 ms, to about 0.63 at TR = 2000 ms. However, while the areas with significantly positive or negative correlations are separated by a relatively narrow diagonal area at TR = 100 ms, the diagonal area with non-significant correlations expands with increasing TR (Fig. 8d-f). At TR = 2000 ms, the area of non-significant correlations about duplicated compared to TR = 1000 ms (Fig. 8f vs. 8e). Qualitatively similar behavior

can be observed for TR variations for scenarios 2 and 3 (data not shown).

In summary: Overall, amplitude changes in CBF and CMRO₂ induce a change in sign with BOLD-FC values changing in a largely linear way, while the dependence of BOLD-FC on temporal delays in CBF and CMRO₂ responses shows more complex behavior with more extended areas of vanishing BOLD-FC especially for long characteristic time constants ($\tau_m, \tau_f > 4$ s). CBF-CBV coupling on the other hand appears to exert only minor influence on observed BOLD-FC. Our simulations also demonstrate that SNR and temporal resolution do not critically influence the dependence on metabolic and hemodynamic parameters but would in practice affect the statistical significance of detecting BOLD-FC.

4. Discussion

Based on dynamic simulations of BOLD signal time curves (BOLD-TCs), elicited by a synthetic neuronal input signal with low frequency amplitude modulations, we demonstrate a crucial impact of neurovascular coupling on BOLD-FC. Specifically, we investigated correlations between simulated BOLD-TCs of defined physiological reference signals used as ‘non-impaired’ seeds, and ‘impaired’ target regions for a wide range of physiological alterations, including prescribed changes in CMRO₂, CBF, CBV *amplitudes, delays and coupling*. The dependence of BOLD-FC on CMRO₂ and CBF amplitudes is straight forward with, at a given CMRO₂ amplitude, an almost linear transition from negative to positive BOLD-FC with increasing CBF amplitude. The influence of CMRO₂ and CBF response delays on BOLD-FC is relatively complex but also gives rise to areas (in the parameter space) with distinct positive and negative BOLD-FC, while CBF-CBV coupling appears to exert rather minor influence. In comparison to tight coupling, a slower CBV response appears to clearly benefit detection of significant BOLD-FC, especially for scenarios 1: amplitude and 3: coupling. In addition, significant effects of SNR and temporal resolution, i.e. TR, on BOLD-FC were present but smaller than those of physiological variables and their change. In summary, to the best of our knowledge, these results provide first evidence – in terms of simulation experiments – that distinct alterations in neurovascular coupling have characteristic effects on BOLD-FC. Data suggest that aberrant BOLD-FC of brain disorders with neurovascular coupling changes such as aberrant perfusion or vascular reactivity, do not only reflect aberrant neural activity but also widely ignored brain vessel and hemodynamic-metabolic physiology.

4.1. Influence of CMRO₂, CBF and CBV amplitudes, delays, coupling, SNR and temporal resolution on BOLD-TCs and BOLD-FC

Calculated BOLD-FC (Fig. 6) distinctly depends on simulated physiological alterations across the three investigated parameter spaces, which are defined by varying CMRO₂ and CBF response *amplitudes* (Scenario 1) and *delays* (Scenario 2) as well as CBF-CBV *coupling* (Scenario 3). In general, observed BOLD-FC is explained by the characteristic BOLD-TCs of both seed and target regions (Figs. 4 and 5, and Supplementary Fig. S1) and especially their temporal or phase relationship. In more detail, our BOLD-signal model yields – in line with previous studies – an increase in BOLD signal relative to baseline, when the CBF increase surpasses the CMRO₂ increase (Ogawa et al., 1993). Otherwise, a CMRO₂ increase surpassing the CBF increase results in a decrease in BOLD signal relative to baseline (Griffith and Buxton, 2011). Along with the slowly oscillating nature of continuous neural input to the neuro-vascular coupling system, continuous oscillatory or fluctuating BOLD signals arise with characteristic phase shifts due to differences in response *amplitudes* (Scenario 1), response *delays* (Scenario 2) or CBF-CBV *coupling* (Scenario 3). With respect to resulting BOLD-FC from seed and target BOLD-TCs, significantly positive or negative BOLD-FC values are observed when the target BOLD-TCs – with sufficiently large amplitudes – are either in phase or in opposite phase with the reference seed BOLD-TCs, respectively. In the following, specific details are discussed for each scenario.

Scenario 1. For CMRO₂ and CBF *amplitude* variations, the relation

between observed BOLD-FC values (Fig. 6a,g) and underlying BOLD-TCs (i.e. seed (Fig. 5a) and targets (Fig. 5b–d)) is especially clear, because they merely affect amplitude and sign of the BOLD signal changes relative to baseline. Accordingly, depending on whether the CBF amplitude surpasses the CMRO₂ amplitude or vice versa, the resulting BOLD signal changes relative to baseline (i.e. BOLD response, as we abbreviate this effect in the following) are either positive or negative, respectively. In line with a more detailed steady-state BOLD signal model (Griffith and Buxton, 2011), BOLD responses vanish for the case of tight coupling, when the CBF-CMRO₂ coupling ratio $n = (f_1 - 1)/(m_1 - 1) \approx 1.3$ (see yellow line in Fig. 6a). For the case of slower CBF-CBV coupling on the other hand, BOLD responses rather vanish for $n \approx 1$. Additional simulations showed that the BOLD signal zero crossing occurs at a CBF-CMRO₂ coupling ratio $n \approx 1$ for CBV time constants $\tau_v \geq 10$ s, where CC-values slightly increase with longer τ_v values (data not shown). This can be understood by considering, that a dynamic model under tight coupling conditions rather behaves like a steady state model, whereas in the case of slower CBV, the delayed CBV response facilitates a faster (somehow uncoupled) CBF-driven BOLD response.

Since the delay constants were chosen identical ($\tau_m = \tau_f = 2$ s), the resulting BOLD-TCs in the target regions (Fig. 5b–d, Supplementary Fig. S1b–d) are always perfectly aligned either in phase (for positive responses) or in opposite phase (for negative responses) to the reference seed BOLD-TC (Fig. 5a, Supplementary Fig. S1a). With respect to BOLD-FC (Fig. 6a,g), this causes two distinct types of areas (in the parameter space) with significantly positive (high CBF amplitudes) and negative (high CMRO₂ amplitudes) BOLD-FC values. The transitional zone of non-significant BOLD-FC along the diagonal, is caused by the amplitudes of the BOLD responses converging to zero (Fig. 5b), where $n \approx 1.3$ or 1 for the cases of tight coupling or slower CBV, respectively (Fig. 6a,g). BOLD-FC also depends on CBF-CBV coupling, (compare Fig. 6a vs. 6g), where a slower CBV response favors a stronger BOLD-FC due to a higher BOLD response; because when the CBV response is too slow to follow the oscillatory input, this rather results in an elevated baseline CBV with only minor temporal changes (compare Fig. 4b vs. 4g). This observation fits previous simulation results (Simon and Buxton, 2015) and supports the notion of Lewis and coworkers (Lewis et al., 2016) that ‘a new vascular baseline’ could favor the detection of faster BOLD dynamics. On the other hand, a slow CBV response may as well favor the detection of BOLD responses to short stimuli (or singular intrinsic neuronal events) when CBF raises quickly, while the delayed CBV response remains small to negligible. This effect can be gleaned from Fig. 4g, when comparing the strong delayed CBV response to the initial 20 s block stimulation vs. the weak CBV oscillations relative to the elevated baseline. This view is supported by results of Drew et al. (Drew et al., 2011; see their Fig. 2) that could qualitatively be reproduced by our simulation model assuming slower CBV conditions (data not shown).

Remarkably, BOLD-FC for target BOLD-TCs that are identical to the reference seed BOLD-TC ($m_1 = 1.25$, $f_1 = 1.5$, indicated by a yellow square in the parameter spaces of CC-values in Figs. 6–8) do not yield highest correlations, suggesting that detection of significantly positive BOLD-FC always benefits from increased CBF response amplitudes, which fits with previous results (Liang et al., 2013). Significantly negative BOLD-FC on the other hand, requires that the CBF response amplitude lies well below the CMRO₂ response amplitude (i.e., $n < 1$, Fig. 6b,e, h,k).

Scenario 2. For CMRO₂ and CBF *delay* variations, the patterns of BOLD-TCs are more complex. At immediate CBF response ($\tau_f = 0.5$ s), the amplitude of BOLD-TCs increases with τ_m and reaches a plateau for $\tau_m > \approx 2.0$ s (Fig. 5). With increasing τ_f , the minimum BOLD response always occurs around $\tau_f \approx \tau_m$, where for $\tau_f > \approx 4.0$ s, the range of τ_m values, leading from small to negligible BOLD responses, increases (see Fig. 5g and h). With respect to BOLD-FC, these patterns of BOLD-TCs result in two distinct types of areas with positive and negative BOLD-FC. Positive BOLD-FCs prevail around $\tau_f \approx [1–2]$ s (for all τ_m) with a clear constriction around $\tau_m \approx [1–2]$ s, where strongest correlation values occur for either

shortest ($\tau_m = 0.5$ s) or prolonged ($\tau_m \approx [3.5\text{--}8]$ s) CMRO₂ delays (Fig. 6b,h). Negative BOLD-FC, on the other hand, centers around $\tau_m \approx [1\text{--}2]$ s for $\tau_f > 3.5$ s. In-between these areas of positive and negative BOLD-FC, slightly above the diagonal (where $\tau_f = \tau_m$) and in the upper right quadrant (where both $\tau_f, \tau_m >\approx 4$ s) exists a (transitional) zone with non-significant BOLD-FC. The extension of areas with significant BOLD-FC is larger for slower CBF-CBV coupling. It is also worth noting that there are areas, especially along the axis, i.e. for $\tau_f = 0.5$ s and $\tau_m = 0.5$ s, where BOLD signal changes are reasonably large but BOLD-FC values are still small and non-significant. In these areas, low BOLD-FC is due to phase shifts between the respective BOLD-TCs and the reference seed. Interestingly, the reference BOLD-TC with identical delays, i.e. $\tau_f = \tau_m = 2$ s, lies close to the regime of non-significant BOLD-FC, implicating that at an presumably normal CBF response delay, detection of BOLD-FC would benefit from either an immediate or a delayed CMRO₂ response in the target region. Whereas, according to our simulations, significant negative BOLD-FC would require a delayed CBF response (Fig. 6b,e,h,k). With respect to the observed pattern, the extension of areas showing negative and positive BOLD-FC values at $\tau_m \approx 2$ s and $\tau_f \approx 2$ s, respectively, implies that their location depends on the reference values assumed for simulations. In addition, the observed pattern in the (τ_f, τ_m) parameter space may also depend on properties of the neuronal input, i.e. periodicity. This issue clearly needs further investigations.

Scenario 3. With respect to CBF-CBV coupling, BOLD-TCs show a rather simple pattern. Specifically, either weak, i.e. low α_v , or delayed CBV responses, i.e. long τ_v (essentially causing an elevated baseline as discussed above), favor large BOLD signal changes for rapidly oscillating stimuli (Fig. 5i-l). This is explained by the fact that synchronous increases in CBV effectively counteract positive BOLD responses (Ogawa et al., 1993). Thus, low CBV changes or an elevated CBV baseline benefit the detection of BOLD-FC for rapidly oscillating signals in accordance with (Lewis et al., 2016; Simon and Buxton, 2015). With respect to BOLD-FC, scenario 3 is characterized by extended areas showing positive correlation, where in contrast to tight coupling, significant BOLD-FC values clearly prevail for the case of slower CBV (Fig. 6c,f,i,l). Only for strong CBF-CBV coupling ($\alpha_v >\approx 0.2$) and $\tau_v <\approx 5$ s those are clearly diminished. With respect to timing aspects, a delayed CBV response is most commonly observed (Hillman et al., 2007; Drew et al., 2011; Kim and Kim, 2011; Simon and Buxton, 2015), but there is recent evidence of Liu and coworkers that CBV might also be following rapid CBF changes (Liu et al., 2019). However, in the light of our simulation results and those of others (Simon and Buxton, 2015; Lewis et al., 2016), low amplitude CBV oscillations could also be observed in the case of delayed CBV response. In either case, since recent results indicate values below 0.2 for α_v (Chen and Pike, 2010; Wesolowski et al., 2019), our results imply that CBF-CBV coupling most likely plays a minor role for the detection of BOLD-FC.

Signal-to-Noise ratio and temporal resolution. The effects of SNR and temporal resolution on BOLD-FC are simple in comparison to the effects of changes in the investigated physiological variables. However, it is important to note that the parameter spaces explored in the current simulation study are relatively broad. Thus, in practical settings, low SNR and temporal resolution might still be highly important factors hindering successful detection of BOLD-FC especially in subjects with rather mild impairments. At lower SNR, the decrease in BOLD-FC values is explained by a higher noise level as compared to the underlying BOLD signal's amplitude (Fig. 7). Regarding the effect of temporal resolution (Fig. 8), absolute BOLD-FC values remained relatively similar across the explored TR values but the areas of non-significant BOLD-FC decreased for higher temporal resolution. This increase in significance in the current simulations was mostly due to an increase in statistical power, as the number of data points increased with increasing sampling rate (i.e., reduced TR). Thus, the influence of SNR and temporal resolution mainly resulted in a parametric modulation of BOLD-FC's strength with decreasing CC-values for both lower SNRs and sampling rates. This behavior is consistent with the strength of functional connectivity values documented with high-field fMRI and at high sampling rates (Setsompop et al., 2016;

Preibisch et al., 2015).

4.2. Implications for BOLD-FC studies in patients with brain diseases causing aberrant neuro-vascular coupling

BOLD-FC is widely applied for studying brain diseases, and alterations in BOLD-FC – both positive and negative – have been reported for a wide range of diseases from neurodegenerative diseases such as Alzheimer's disease to neuropsychiatric disorders such as schizophrenia or major depression (Zhou et al., 2010; Lim et al., 2014; Greicius et al., 2004; Sorg et al., 2007; Zhang and Raichle, 2010; Manoliu et al., 2014; Avram et al., 2018; Brandl et al., 2019). Most of these BOLD-FC changes have been interpreted as changes in the underlying neuronal activity or in connectivity between brain areas. Our results, however, suggest that aberrant BOLD-FC in disorders associated with significant hemodynamic-metabolic changes might be explained at least partly by concomitant hemodynamic-metabolic changes. Remarkably, hemodynamic-metabolic changes have been independently demonstrated for most of above-mentioned disorders from Alzheimer's disease (Alexopoulos et al., 2012; Ostergaard et al., 2013; Riederer et al., 2018) to schizophrenia (for review (Katsel et al., 2017)), suggesting that aberrant BOLD-FC might be partly linked with aberrant hemodynamic-metabolic brain features. This link underscores the high relevance of accounting for hemodynamic and metabolic changes in studies of neuropsychiatric disorders.

In more detail, our simulation results demonstrate distinct changes of seed-based BOLD-FC when CMRO₂, CBF and CBV amplitudes, delays and coupling in the target regions deviate from the 'non-impaired' reference BOLD-TC. Reduced CMRO₂ and CBF response amplitudes can be expected in pathologies where brain tissues are restricted in their ability to adapt either oxygen metabolism or perfusion to increased metabolic demands. This is likely to be the case in either neurodegenerative (Iadecola, 2004; Fleisher et al., 2009; Alexopoulos et al., 2012; Peca et al., 2013; Riederer et al., 2018; Göttsler et al., 2019) or vascular diseases (Derdeyn et al., 2002; Bouvier et al., 2015; De Vis, Petersen et al., 2015; Gersing et al., 2015; Cogswell et al., 2017; De Vis, Bhogal et al., 2018; Göttsler et al., 2019), where reduced oxygen and glucose metabolism as well as a reduced cerebrovascular reactivity has been detected. Recent studies also provided first evidence that physiological changes, i.e. reductions in CVR and CBF, indeed contribute to explaining BOLD-FC changes observed in patients with Moyamoya disease (Liu et al., 2017) and Alzheimer's disease (Göttsler et al., 2019). From animal studies, there is also evidence that cerebral glucose consumption during somatosensory stimulation is not altered when CBF response is blocked (Cholet et al., 1997), implying intact neuronal activity might be present in spite of perfusion impairments. According to our simulation results (Fig. 6a,g), it is likely that reductions in BOLD-FC, reported in patients with reduced perfusion and CVR are at least in part due to exhausted vascular reserve capacity. Based on our results, one might also hypothesize that reduced oxygen consumption at preserved CVR would induce highly significant positive BOLD-FC, conditions that might be fulfilled in schizophrenia (Katsel et al., 2017).

Alterations in CMRO₂ and CBF responses delays can likewise be expected to occur in neurodegenerative or vascular diseases, where especially delays in perfusion have frequently been reported (Kawano et al., 2016; Khalil et al., 2017; Richter et al., 2017; De Vis, Bhogal et al., 2018; Kaczmarz et al., 2018). Recent work also provided evidence that flow-metabolism coupling is altered even in individuals with asymptomatic vascular disease (Göttsler et al., 2019). According to our simulations, delayed perfusion, i.e. increased CBF response delay τ_f , would cause reduced and finally negative BOLD-FC (Fig. 6b,h). By comparing cross correlation-based delay analyses of rs-fMRI to contrast agent based measures, arterial delays up to 9s have been demonstrated in patients with Moyamoya disease (Christen et al., 2015) and stroke (Lv et al., 2013). Interestingly, accounting for vascular delays was found to impact on BOLD-FC in Moyamoya patients (Christen et al., 2015) as well as

healthy subjects (Chang et al., 2008). A delay in CMRO₂ response, on the other hand, would rather imply stronger positive BOLD-FC. While there is some evidence that post stimulus undershoots lasting for tens of seconds in task fMRI might also be caused by prolonged elevation of CMRO₂ instead of elevated CBV alone (Hua et al., 2011; Mullinger et al., 2017), a pathological delay in CMRO₂ response, however, would be much more difficult to substantiate.

Alterations in CBF-CBV coupling, i.e. reduced CBV responses, would be expected to occur in brain tissues with exhausted vascular reserve capacity, while long delays might be present in areas with delayed perfusion due to vessel occlusions (De Vis, Petersen et al., 2015; Kawano et al., 2016; Cogswell et al., 2017; Richter et al., 2017; De Vis, Bhogal et al., 2018; Kaczmarz et al., 2018). According to our simulations, reduced amplitudes and long delays of CBV responses would rather benefit detection of BOLD-FC, since our simulations yield significant positive BOLD-FC across almost the entire parameter space (Fig. 6c,f,i,l).

Taken together, our results imply that BOLD-FC is most likely compromised in a number of pathophysiological conditions that go along with alterations especially in CMRO₂ and CBF response amplitudes and delays. Thus, an interpretation with respect to underlying neuronal activity might be misleading and measures to account for neurovascular coupling alterations need to be taken in order to improve fidelity of BOLD-FC and disentangle the vascular from the neural contributions, especially in pathology.

Since the BOLD signal depends on the interplay of CBF and CMRO₂, its quantitative interpretation crucially depends on a better understanding of energy metabolism (Herman et al., 2009; Buxton, 2010; Hyder et al., 2011; Hyder and Rothman, 2012; Hyder et al., 2013). One possibility might be an absolute quantification of oxygen metabolism, which besides ¹⁵O-based positron emission tomography (Leenders et al., 1990; Ishii et al., 1996; Ito et al., 2004; Ibaraki et al., 2008), would also be possible with more accessible MRI techniques either based on gas challenges, i.e. dual-calibrated fMRI (Gauthier and Hoge, 2013; Wise et al., 2013; Merola et al., 2016; Germuska et al., 2019; Germuska and Wise, 2019) or quantification of the BOLD effect (Yablonskiy and Haacke, 1994; Yablonskiy, 1998; Qin et al., 2011; Guo and Wong, 2012; Lu et al., 2012; Christen et al., 2013; Hirsch et al., 2014; Stone and Blockley, 2017). However, measurement of absolute CMRO₂ is challenging, and current methods either suffer from missing spatial (Qin et al., 2011; Guo and Wong, 2012; Lu et al., 2012) or temporal resolution (Christen et al., 2013; Hirsch et al., 2014; Stone and Blockley, 2017).

4.3. Issues regarding the validity of neuronal and BOLD signal modeling for resting-state BOLD-FC

How biologically realistic is our model approach simulating the influence of metabolic-hemodynamic coupling on BOLD-FC?

Neuronal input model – signal generation, slow oscillations, and neural FC. All of our simulations are based on a simple synthetic input signal with low frequency amplitude modulations as *neuronal input*. This simplified model ignores a more detailed neuronal basis of BOLD signal time curves and eventually BOLD-functional connectivity. Recent studies use more realistic models to simulate the underlying neural activity underpinning resting state BOLD-TCs or derived BOLD-FC (Ritter et al., 2013; Zalesky et al., 2014; Sanz-Leon et al., 2015; Schirner et al., 2018). Furthermore, we did not realistically account for (infra-) slow neural fluctuations; instead, we realized slow fluctuations by 0.05 Hz amplitude modulation of faster oscillations. Based on the observed spectrum of dynamical regimes and timescales in spontaneous cortical activity (Sanchez-Vives and Mattia, 2014) and in particularly its functional connectivity, coherent slow neural fluctuations are discussed to be generated either by synchronicity of remote fluctuations and/or by phase co-activity of propagating global waves (Matsui et al., 2016; Mitra et al., 2018). We justify our simplified approach of neuronal input modeling because the major focus of our study is on the investigation of the impact of profound hemodynamic impairments on BOLD-FC. Nevertheless, the

interplay between neuronal and hemodynamic impairments clearly needs further investigation, which requires more realistically generated neuronal input signals.

BOLD-signal model

(i) *Task-based BOLD signal model:* With respect to *dynamic simulations of the BOLD signal*, we use a rather simple model that was conceived for modeling BOLD-fMRI responses to *tasks* (Buxton et al., 1998; Buxton et al., 2004; Obata et al., 2004; Simon and Buxton, 2015). In contrast to Simon and Buxton (2015) who successfully modeled the dynamic behaviors of rapidly oscillating signals accounting for extravascular signal contributions only, we decided to employ the BOLD signal model derived by Obata et al. (Obata et al., 2004) that additionally includes intravascular contributions. This model is thought to better fit the reality because at 3T extravascular contributions account for only about 70% of the observed BOLD signal changes (Li and van Zijl, 2020). However, this advantage might not take full effect because additional model parameters are needed that are not really well known. Therefore, we additionally performed simulations using the purely extravascular signal model as employed by Simon and Buxton (2015) (see supplementary material). A direct comparison shows that the overall patterns are similar, which increases confidence in the general validity of our results. Nevertheless, further studies with more refined and well-defined models are needed. For example, the extension of a more detailed steady state signal model (Griffith and Buxton, 2011) to dynamic simulations would perhaps reveal additional effects and produce other interesting dynamics. Furthermore, there are a number of other hemodynamic models that might also be considered, e.g. (Friston et al., 2000; Behzadi and Liu, 2005; Kong et al., 2004).

Furthermore, we assume parameters for modeling presumably healthy BOLD-responses to rapidly oscillating stimuli that were derived from observations of task responses in healthy subjects (Simon and Buxton, 2015). Buxton et al. (Buxton et al., 2014) noted that variations of the CBF-CMRO₂ coupling ratio n have a strong effect on observed BOLD responses. Based on findings of quantitative fMRI studies, they claim that an empirical pattern appears to emerge: (1) if stimuli are modulated to create a stronger response (e.g., increasing stimulus contrast), CBF is modulated more than CMRO₂; (2) if the brain state is altered such that the response to the same stimulus increases (e.g., by modulating attention, adaptation, stimulus contrast, or excitability), CMRO₂ is modulated more than CBF. These findings lead them to speculate that the variability of the CBF-CMRO₂ coupling ratio may reflect different proportions of inhibitory and excitatory evoked activity, potentially providing a new window on neural activity in the human brain. These issues are potentially also relevant for the neurovascular coupling in the context of spontaneous ongoing neuronal activity.

(ii) *Resting-state BOLD fluctuations:* While there is an ongoing debate how *intrinsic BOLD activity* relates to underlying electrical neuronal activity, there are strong indications that BOLD signal changes caused by underlying spontaneous electrical activity, are indeed caused by mechanisms similar to task-based fMRI. More precisely, spontaneous increases in neuronal activity have been shown to precede increases in arteriolar diameter (Mateo et al., 2017) and BOLD signal (He et al., 2018). This indicates that assuming a positive BOLD signal coupling to spontaneous neuronal activity is reasonable. In animal studies, Mateo (Mateo et al., 2017) and He (He et al., 2018) found time lags of about 2 s between the increase of electrical neuronal activity and increases of arteriolar diameter or CBV, respectively, while venular BOLD response was slightly more delayed (2.30 ± 0.19 s and 1.76 ± 0.14 s) (He et al., 2018). This indicates that intrinsic neuronal activity might elicit rather fast hemodynamic responses at rest. Faster hemodynamic responses were also detected by Lewis et al. (Lewis et al., 2016) when investigating BOLD signal changes elicited by contrast modulated visual stimuli at 0.2 Hz, 0.33 Hz, and 0.5 Hz. Based on biophysical model simulations, their results could be explained if rapidly varying stimuli elicit faster BOLD responses (Lewis et al., 2016), which also fits with previous results of (Simon and Buxton, 2015) and very recent work of Kim et al., 2019.

While these previous studies suggest rather rapid hemodynamic responses, there is limited data available on the specific changes of CMRO₂ as well as CBF and CBV amplitudes and delays in pathology. While it appears plausible, that vascular and neurodegenerative diseases induce metabolic and vascular impairments causing conditions with vanishing CMRO₂ and CBF response amplitudes, there is less reliable information with respect to delay constants. While macrovascular perfusion delays up to 9s have been observed in Moyamoya disease (Christen et al., 2015) and stroke (Lv et al., 2013), it is not clear whether and how delays on the microvascular level, as for example demonstrated by (Chow et al., 2020), might additionally influence BOLD-FC. Much more difficult to obtain is information on metabolic time constants. To the best of our knowledge, we could not find any information about that. Therefore, we chose a rather wide range of temporal dynamics for CMRO₂ as well as CBF and CBV amplitudes and delays to cover the range of potential pathophysiological alterations as comprehensively as possible. Our results indicate that especially the slower CBF-CBV coupling scenarios essentially introduce a baseline shift in CBV that benefits the detection of rapidly oscillating synthetic neuronal inputs. This fits with indications that CBF-CBV coupling plays a minor role in the vascular response to either short (Kim et al., 2019) or rapidly oscillating stimuli (Lewis et al., 2016), which could be considered predictive for hemodynamic responses elicited by intrinsic neuronal activity.

(iii) *Steady state resting-state BOLD-model:* Our simulations rely on a model that strictly assumes changes in neuronal activity as increases from a pre-stimulus baseline, while Bennett et al. propose a model (Bennett et al., 2018), which more directly relates the BOLD signal to neuronal activity, both above and below baseline (Bennett et al., 2018). This allows to better account for transient BOLD signals especially with regard to detailed investigations on the role neuronal activity can play with regard to post-stimulus undershoot and overshoots. Their relation of CMRO₂ to mean neuronal firing rate is based on previous work (Hyder et al., 2013). This influence of neural activity levels without stimulation certainly needs to be studied in more detail for example by implementing such models within more realistic neural simulation frameworks (Sanz-Leon et al., 2015).

Modeling confounds. Our simulations completely ignore the influence of additional confounding factors with regard to BOLD-FC such as cardiac and respiration-related fluctuations (Birn et al., 2006; Chang and Glover, 2009; Whittaker et al., 2019), macrovascular contributions (Tak et al., 2015; Zhu et al., 2015), and other sources (Triantafyllou et al., 2011). We expect that the introduction of structured noise causes additional spurious correlations and interactions with the described effects of impaired physiology. For cardiac and respiratory confounds, complex interactions are especially expected at commonly used TRs of 1s to 2s, and in areas of the parameter space where correlations due to the prescribed neuronal input vanish, e.g. where $n \approx 1-1.3$. While these issues certainly also deserve closer investigation, and simulation approaches offer the possibility to relatively easily explore for example the influence of TR, the investigation of related effects lies beyond the scope of this study.

Spatial aspects. In this work, we did not consider any spatial aspects of BOLD-FC though spatiotemporal dynamics are crucial for the emergence of local and global brain networks at rest (Melie-Garcia, Sanabria-Diaz and Sánchez-Catásus, 2012; Ruiz-Rizzo et al., 2020). We opted not to include spatial information to limit the number of factors that might influence CC-values, thus enabling a closer characterization of rather local hemodynamic and metabolic effects of neurovascular coupling on BOLD-FC. However, it is known that CBF exhibits non-homogeneous changes across brain areas in healthy subjects generating characteristic brain patterns (De Luca, Beckmann et al., 2006). Furthermore, it has been reported that spatial CBF connectivity patterns are specifically altered in brain pathology. For example, patients with schizophrenia have been shown to exhibit regionally increased and decreased CBF values as well as group-specific brain network topology

changes compared to healthy controls and their non-affected first-grade relatives, respectively (Cui et al., 2017). These findings emphasize the relevance of exploring spatial aspects of CBF and CMRO₂ dynamics, especially since several networks, e.g. attention and default mode, are supplied via different flow territories, which may also change the timing of CBF fluctuations via different arrival times and their respective network topologies.

5. Conclusion

Our results demonstrate that alterations in neurovascular coupling are relevant for aberrant resting-state BOLD-FC. The pronounced effects of metabolic and vascular dynamics on BOLD-FC as demonstrated by our current modeling study emphasize the necessity to better characterize metabolic-hemodynamic impairments. A more thorough understanding of these alterations will improve the interpretation of BOLD-FC studies in general, and in particular in pathology. At the current state, our recommendation would be to complement BOLD-FC studies, at least of at-risk patient populations, with perfusion and oxygenation sensitive MRI, and to additionally consider this hemodynamic-metabolic information when interpreting BOLD-FC results. In cases where this is not available, we recommend careful interpretation of BOLD-FC results considering previous findings about hemodynamic-metabolic changes. In our opinion, accurate modeling of the hemodynamic-metabolic context will be important for a better understanding of the interplay between neuronal-vascular-hemodynamic components of intrinsic BOLD-FC and, particularly, for the evaluation of aberrant BOLD-FC in brain diseases with vascular-hemodynamic impairments.

Funding

This work was supported by the German Research Foundation DFG [grant numbers PR 1039/6-1, SO 1336/4-1].

Data/code availability

Data and custom Matlab Code is available at <https://zenodo.org/record/3773316>.

Custom Matlab code used for the BOLD simulations is available at https://gitlab.lrz.de/nmrm_lab/public_projects/bold-simulation.

Ethical approval

Not applicable.

Informed consent

Not applicable.

Author contributions

Conception and design of the study: MEAM, CS, CP; simulations of electrophysiology: MEAM; simulations of BOLD signal: CP; analysis and interpretation of data: MEAM, CS, CP; drafting the article: MEAM, CS, CP; revising the article critically for important intellectual content: MEAM, CS, CP; final approval of the version to be submitted: MEAM, CS, CP.

Declaration of competing interest

The authors declare that they have no conflict of interest.

CRediT authorship contribution statement

Mario E. Archila-Meléndez: Writing - original draft. **Christian Sorg:** Writing - original draft. **Christine Preibisch:** Writing - original draft.

Acknowledgements

The authors thank the German Research Foundation DFG [grant numbers PR 1039/6-1, SO 1336/4-1] for funding.

Appendix A. Supplementary data

Supplementary data to this article can be found online at <https://doi.org/10.1016/j.neuroimage.2020.116871>.

References

- Alexopoulos, P., Sorg, C., Forschler, A., Grimmer, T., Skokou, M., Wohlschlager, A., Perneckezy, R., Zimmer, C., Kurz, A., Preibisch, C., 2012. Perfusion abnormalities in mild cognitive impairment and mild dementia in Alzheimer's disease measured by pulsed arterial spin labeling MRI. *Eur. Arch. Psychiatr. Clin. Neurosci.* 262 (1), 69–77.
- Ances, B.M., Liang, C.L., Leontiev, O., Perthen, J.E., Fleisher, A.S., Lansing, A.E., Buxton, R.B., 2009. Effects of aging on cerebral blood flow, oxygen metabolism, and blood oxygenation level dependent responses to visual stimulation. *Hum. Brain Mapp.* 30 (4), 1120–1132.
- Avram, M., Brandl, F., Bauml, J., Sorg, C., 2018. Cortico-thalamic hypo- and hyperconnectivity extend consistently to basal ganglia in schizophrenia. *Neuropsychopharmacology* 43 (11), 2239–2248.
- Bandettini, P.A., 2014. Neuronal or hemodynamic? Grappling with the functional MRI signal. *Brain Connect.* 4 (7), 487–498.
- Bastos, A.M., Usrey, W.M., Adams, R.A., Mangun, G.R., Fries, P., Friston, K.J., 2012. Canonical microcircuits for predictive coding. *Neuron* 76 (4), 695–711.
- Behzadi, Y., Liu, T.T., 2005. An arteriolar compliance model of the cerebral blood flow response to neural stimulus. *Neuroimage* 25 (4), 1100–1111.
- Bennett, M.R., Farnell, L., Gibson, W.G., 2018. Quantitative relations between BOLD responses, cortical energetics, and impulse firing. *J. Neurophysiol.* 119 (3), 979–989.
- Birn, R.M., Diamond, J.B., Smith, M.A., Bandettini, P.A., 2006. Separating respiratory-variation-related fluctuations from neuronal-activity-related fluctuations in fMRI. *Neuroimage* 31 (4), 1536–1548.
- Biswal, B., Yetkin, F.Z., Haughton, V.M., Hyde, J.S., 1995. Functional connectivity in the motor cortex of resting human brain using echo-planar MRI. *Magn. Reson. Med.* 34 (4), 537–541.
- Blicher, J.U., Stagg, C.J., O'Shea, J., Ostergaard, L., MacIntosh, B.J., Johansen-Berg, H., Jezzard, P., Donahue, M.J., 2012. Visualization of altered neurovascular coupling in chronic stroke patients using multimodal functional MRI. *J. Cerebr. Blood Flow Metabol.* 32 (11), 2044–2054.
- Blockley, N.P., Francis, S.T., Gowland, P.A., 2009. Perturbation of the BOLD response by a contrast agent and interpretation through a modified balloon model. *Neuroimage* 48 (1), 84–93.
- Blockley, N.P., Griffeth, V.E., Simon, A.B., Buxton, R.B., 2013. A review of calibrated blood oxygenation level-dependent (BOLD) methods for the measurement of task-induced changes in brain oxygen metabolism. *NMR Biomed.* 26 (8), 987–1003.
- Bouvier, J., Detante, O., Tahon, F., Attye, A., Perret, T., Chechin, D., Barbieux, M., Boubagra, K., Garambois, K., Tropres, I., Grand, S., Barbier, E.L., Krainik, A., 2015. Reduced CMRO₂ and cerebrovascular reserve in patients with severe intracranial arterial stenosis: a combined multiparametric qBOLD oxygenation and BOLD fMRI study. *Hum. Brain Mapp.* 36 (2), 695–706.
- Brandl, F., Avram, M., Weise, B., Shang, J., Simoes, B., Bertram, T., Hoffmann Ayala, D., Penzel, N., Gursel, D.A., Bauml, J., Wohlschlager, A.M., Vukadinovic, Z., Koutsoularis, N., Leucht, S., Sorg, C., 2019. Specific substantial dysconnectivity in schizophrenia: a transdiagnostic multimodal meta-analysis of resting-state functional and structural magnetic resonance imaging studies. *Biol. Psychiatr.* 85 (7), 573–583.
- Brosch, M., Budinger, E., Scheich, H., 2002. Stimulus-related gamma oscillations in primate auditory cortex. *J. Neurophysiol.* 87 (6), 2715–2725.
- Buxton, R.B., 2010. Interpreting oxygenation-based neuroimaging signals: the importance and the challenge of understanding brain oxygen metabolism. *Front. Neuroenergetics* 2, 8.
- Buxton, R.B., Griffeth, V.E., Simon, A.B., Moradi, F., Shmuel, A., 2014. Variability of the coupling of blood flow and oxygen metabolism responses in the brain: a problem for interpreting BOLD studies but potentially a new window on the underlying neural activity. *Front. Neurosci.* 8, 139.
- Buxton, R.B., Uludag, K., Dubowitz, D.J., Liu, T.T., 2004. Modeling the hemodynamic response to brain activation. *Neuroimage* 23 (Suppl. 1), S220–233.
- Buxton, R.B., Wong, E.C., Frank, L.R., 1998. Dynamics of blood flow and oxygenation changes during brain activation: the balloon model. *Magn. Reson. Med.* 39 (6), 855–864.
- Chang, C., Glover, G.H., 2009. Relationship between respiration, end-tidal CO₂, and BOLD signals in resting-state fMRI. *Neuroimage* 47 (4), 1381–1393.
- Chang, C., Thomason, M.E., Glover, G.H., 2008. Mapping and correction of vascular hemodynamic latency in the BOLD signal. *Neuroimage* 43 (1), 90–102.
- Chen, J.J., 2018. Cerebrovascular-reactivity mapping using MRI: considerations for alzheimer's disease. *Front. Aging Neurosci.* 10, 170.
- Chen, J.J., Pike, G.B., 2010. MRI measurement of the BOLD-specific flow-volume relationship during hypercapnia and hypocapnia in humans. *Neuroimage* 53 (2), 383–391.
- Chiarelli, P.A., Bulte, D.P., Wise, R., Gallichan, D., Jezzard, P., 2007. A calibration method for quantitative BOLD fMRI based on hyperoxia. *Neuroimage* 37 (3), 808–820.
- Cholet, N., Seylaz, J., Lacombe, P., Bonvento, G., 1997. Local uncoupling of the cerebrovascular and metabolic responses to somatosensory stimulation after neuronal nitric oxide synthase inhibition. *J. Cerebr. Blood Flow Metabol.* 17 (11), 1191–1201.
- Chow, B.W., Nuñez, V., Kaplan, L., Granger, A.J., Bistrong, K., Zucker, H.L., Kumar, P., Sabatini, B.L., Gu, C., 2020. Caveolae in CNS arterioles mediate neurovascular coupling. *Nature* 579 (7797), 106–110.
- Christen, T., Bolar, D.S., Zaharchuk, G., 2013. Imaging brain oxygenation with MRI using blood oxygenation approaches: methods, validation, and clinical applications. *AJNR Am J Neuroradiol* 34 (6), 1113–1123.
- Christen, T., Jahanian, H., Ni, W.W., Qiu, D., Moseley, M.E., Zaharchuk, G., 2015. Noncontrast mapping of arterial delay and functional connectivity using resting-state functional MRI: a study in Moyamoya patients. *J. Magn. Reson. Imag.* 41 (2), 424–430.
- Cogswell, P.M., Davis, T.L., Strother, M.K., Faraco, C.C., Scott, A.O., Jordan, L.C., Fusco, M.R., Frederick, B.D., Hendrikse, J., Donahue, M.J., 2017. Impact of vessel wall lesions and vascular stenoses on cerebrovascular reactivity in patients with intracranial stenotic disease. *J. Magn. Reson. Imag.* 46 (4), 1167–1176.
- Cui, L.B., Wang, L.X., Tian, P., Wang, H.N., Cai, M., Guo, F., Li, C., Wu, Y.J., Qiao, P.G., Xu, Z.L., Liu, L., He, H., Wu, W.J., Xi, Y.B., Yin, H., 2017. Aberrant perfusion and its connectivity within default mode network of first-episode drug-naïve schizophrenia patients and their unaffected first-degree relatives. *Sci. Rep.* 7, 16201.
- Davis, T.L., Kwong, K.K., Weisskoff, R.M., Rosen, B.R., 1998. Calibrated functional MRI: mapping the dynamics of oxidative metabolism. *Proc. Natl. Acad. Sci. U. S. A.* 95 (4), 1834–1839.
- De Luca, M., Beckmann, C.F., De Stefano, N., Matthews, P.M., Smith, S.M., 2006. fMRI resting state networks define distinct modes of long-distance interactions in the human brain. *Neuroimage* 29 (4), 1359–1367.
- De Vis, J.B., Bhogal, A.A., Hendrikse, J., Petersen, E.T., Siero, J.C.W., 2018. Effect sizes of BOLD CVR, resting-state signal fluctuations and time delay measures for the assessment of hemodynamic impairment in carotid occlusion patients. *Neuroimage* 179, 530–539.
- De Vis, J.B., Hendrikse, J., Bhogal, A., Adams, A., Kappelle, L.J., Petersen, E.T., 2015. Age-related changes in brain hemodynamics: A calibrated MRI study. *Hum. Brain Mapp.* 36 (10), 3973–3987.
- De Vis, J.B., Petersen, E.T., Bhogal, A., Hartkamp, N.S., Klijn, C.J., Kappelle, L.J., Hendrikse, J., 2015. Calibrated MRI to evaluate cerebral hemodynamics in patients with an internal carotid artery occlusion. *J. Cerebr. Blood Flow Metabol.* 35 (6), 1015–1023.
- Derdeyn, C.P., Videen, T.O., Yundt, K.D., Fritsch, S.M., Carpenter, D.A., Grubb, R.L., Powers, W.J., 2002. Variability of cerebral blood volume and oxygen extraction: stages of cerebral haemodynamic impairment revisited. *Brain* 125 (Pt 3), 595–607.
- Drew, P.J., Shih, A.Y., Kleinfeld, D., 2011. Fluctuating and sensory-induced vasodynamics in rodent cortex extend arteriole capacity. *Proc. Natl. Acad. Sci. U. S. A.* 108 (20), 8473–8478.
- Engel, A.K., Gerloff, C., Hilgetag, C.C., Nolte, G., 2013. Intrinsic coupling modes: multiscale interactions in ongoing brain activity. *Neuron* 80 (4), 867–886.
- Fleisher, A.S., Podraza, K.M., Bangen, K.J., Taylor, C., Sherzai, A., Sidhar, K., Liu, T.T., Dale, A.M., Buxton, R.B., 2009. Cerebral perfusion and oxygenation differences in Alzheimer's disease risk. *Neurobiol. Aging* 30 (11), 1737–1748.
- Fox, M.D., Raichle, M.E., 2007. Spontaneous fluctuations in brain activity observed with functional magnetic resonance imaging. *Nat. Rev. Neurosci.* 8 (9), 700–711.
- Friston, K.J., Mechelli, A., Turner, R., Price, C.J., 2000. Nonlinear responses in fMRI: the Balloon model, Volterra kernels, and other hemodynamics. *Neuroimage* 12 (4), 466–477.
- Gauthier, C.J., Hoge, R.D., 2013. A generalized procedure for calibrated MRI incorporating hyperoxia and hypercapnia. *Hum. Brain Mapp.* 34 (5), 1053–1069.
- Germuska, M., Chandler, H.L., Stickland, R.C., Foster, C., Fasano, F., Okell, T.W., Steventon, J., Tomassini, V., Murphy, K., Wise, R.G., 2019. Dual-calibrated fMRI measurement of absolute cerebral metabolic rate of oxygen consumption and effective oxygen diffusivity. *Neuroimage* 184, 717–728.
- Germuska, M., Wise, R.G., 2019. Calibrated fMRI for mapping absolute CMRO₂: practicalities and prospects. *Neuroimage* 187, 145–153.
- Gersing, A.S., Ankenbrink, M., Schwaiger, B.J., Toth, V., Janssen, I., Kooijman, H., Wunderlich, S., Bauer, J.S., Zimmer, C., Preibisch, C., 2015. Mapping of cerebral metabolic rate of oxygen using dynamic susceptibility contrast and blood oxygen level dependent MR imaging in acute ischemic stroke. *Neuroradiology* 57 (12), 1253–1261.
- Golestan, A.M., Kwinta, J.B., Strother, S.C., Khatamian, Y.B., Chen, J.J., 2016. The association between cerebrovascular reactivity and resting-state fMRI functional connectivity in healthy adults: the influence of basal carbon dioxide. *Neuroimage* 132, 301–313.
- Göttler, J., Kaczmarz, S., Kallmayer, M., Wustrow, I., Eckstein, H.H., Zimmer, C., Sorg, C., Preibisch, C., Hyder, F., 2019a. Flow-metabolism uncoupling in patients with asymptomatic unilateral carotid artery stenosis assessed by multi-modal magnetic resonance imaging. *J. Cerebr. Blood Flow Metabol.* 39 (11), 2132–2143.
- Göttler, J., Preibisch, C., Riederer, I., Pasquini, L., Alexopoulos, P., Bohn, K.P., Yakushev, I., Beller, E., Kaczmarz, S., Zimmer, C., Grimmer, T., Drzezga, A., Sorg, C., 2019b. Reduced blood oxygenation level dependent connectivity is related to hypoperfusion in Alzheimer's disease. *J. Cerebr. Blood Flow Metabol.* 39 (7), 1314–1325.
- Greicius, M.D., Srivastava, G., Reiss, A.L., Menon, V., 2004. Default-mode network activity distinguishes Alzheimer's disease from healthy aging: evidence from functional MRI. *Proc. Natl. Acad. Sci. U. S. A.* 101 (13), 4637–4642.

- Griffeth, V.E., Buxton, R.B., 2011. A theoretical framework for estimating cerebral oxygen metabolism changes using the calibrated-BOLD method: modeling the effects of blood volume distribution, hematocrit, oxygen extraction fraction, and tissue signal properties on the BOLD signal. *Neuroimage* 58 (1), 198–212, 2011 Sep. 1.
- Grubb Jr., R.L., Raichle, M.E., Eichling, J.O., Ter-Pogossian, M.M., 1974. The effects of changes in PaCO₂ on cerebral blood volume, blood flow, and vascular mean transit time. *Stroke* 5 (5), 630–639.
- Guo, J., Wong, E.C., 2012. Venous oxygenation mapping using velocity-selective excitation and arterial nulling. *Magn. Reson. Med.* 68 (5), 1458–1471.
- Havlicek, M., Roebroek, A., Friston, K.J., Gardumi, A., Ivanov, D., Uludag, K., 2017. On the importance of modeling fMRI transients when estimating effective connectivity: a dynamic causal modeling study using ASL data. *Neuroimage* 155, 217–233.
- He, Y., Wang, M., Chen, X., Pohmann, R., Polimeni, J.R., Scheffler, K., Rosen, B.R., Kleinfeld, D., Yu, X., 2018. Ultra-slow single-vessel BOLD and CBV-based fMRI spatiotemporal dynamics and their correlation with neuronal intracellular calcium signals. *Neuron* 97 (4), 925–939 e925.
- Herman, P., Sanganahalli, B.G., Blumenfeld, H., Hyder, F., 2009. Cerebral oxygen demand for short-lived and steady-state events. *J. Neurochem.* 109 (Suppl. 1), 73–79.
- Hillman, E.M., Devor, A., Bouchard, M.B., Dunn, A.K., Krauss, G.W., Skoch, J., Bacskai, B.J., Dale, A.M., Boas, D.A., 2007. Depth-resolved optical imaging and microscopy of vascular compartment dynamics during somatosensory stimulation. *Neuroimage* 35 (1), 89–104.
- Hirano, Y., Stefanovic, B., Silva, A.C., 2011. Spatiotemporal evolution of the functional magnetic resonance imaging response to ultrashort stimuli. *J. Neurosci.* 31 (4), 1440–1447.
- Hirsch, N.M., Toth, V., Forschner, A., Kooijman, H., Zimmer, C., Preibisch, C., 2014. Technical considerations on the validity of blood oxygenation level-dependent-based MR assessment of vascular deoxygenation. *NMR Biomed.* 27 (7), 853–862.
- Hoge, R.D., 2012. Calibrated fMRI. *Neuroimage* 62 (2), 930–937.
- Hua, J., Stevens, R.D., Huang, A.J., Pekar, J.J., van Zijl, P.C., 2011. Physiological origin for the BOLD poststimulus undershoot in human brain: vascular compliance versus oxygen metabolism. *J. Cerebr. Blood Flow Metabol.* 31 (7), 1599–1611.
- Hyder, F., Herman, P., Sanganahalli, B.G., Coman, D., Blumenfeld, H., Rothman, D.L., 2011. Role of ongoing, intrinsic activity of neuronal populations for quantitative neuroimaging of functional magnetic resonance imaging-based networks. *Brain Connect.* 1 (3), 185–193.
- Hyder, F., Rothman, D.L., 2012. Quantitative fMRI and oxidative neuroenergetics. *Neuroimage* 62 (2), 985–994.
- Hyder, F., Rothman, D.L., Bennett, M.R., 2013. Cortical energy demands of signaling and nonsignaling components in brain are conserved across mammalian species and activity levels. *Proc. Natl. Acad. Sci. U. S. A.* 110 (9), 3549–3554.
- Hyder, F., Shu, C.Y., Herman, P., Sanganahalli, B.G., Coman, D., Rothman, D.L., 2013. CMRO₂ Mapping by Calibrated fMRI: Quantifying Morphology and Physiology of the Human Body Using MRI. L. T. Muftuler, Taylor & Francis Group, LLC.
- Iadecola, C., 2004. Neurovascular regulation in the normal brain and in Alzheimer's disease. *Nat. Rev. Neurosci.* 5 (5), 347–360.
- Ibaraki, M., Miura, S., Shimosegawa, E., Sugawara, S., Mizuta, T., Ishikawa, A., Amano, M., 2008. Quantification of cerebral blood flow and oxygen metabolism with 3-dimensional PET and 15O: validation by comparison with 2-dimensional PET. *J. Nucl. Med.* 49 (1), 50–59.
- Ishii, K., Sasaki, M., Kitagaki, H., Sakamoto, S., Yamaji, S., Maeda, K., 1996. Regional difference in cerebral blood flow and oxidative metabolism in human cortex. *J. Nucl. Med.* 37 (7), 1086–1088.
- Ito, H., Kanno, I., Kato, C., Sasaki, T., Ishii, K., Ouchi, Y., Iida, A., Okazawa, H., Hayashida, K., Tsuyuguchi, N., Ishii, K., Kuwabara, Y., Senda, M., 2004. Database of normal human cerebral blood flow, cerebral blood volume, cerebral oxygen extraction fraction and cerebral metabolic rate of oxygen measured by positron emission tomography with 15O-labelled carbon dioxide or water, carbon monoxide and oxygen: a multicentre study in Japan. *Eur. J. Nucl. Med. Mol. Imag.* 31 (5), 635–643.
- Jensen, O., Mazaheri, A., 2010. Shaping functional architecture by oscillatory alpha activity: gating by inhibition. *Front. Hum. Neurosci.* 4, 186.
- Kaczmarz, S., Grieve, V., Preibisch, C., Kallmayer, M., Helle, M., Wustrow, I., Petersen, E.T., Eckstein, H.H., Zimmer, C., Sorg, C., Göttsche, J., 2018. Increased variability of watershed areas in patients with high-grade carotid stenosis. *Neuroradiology* 60 (3), 311–323.
- Katsel, P., Roussos, P., Pletnikov, M., Haroutunian, V., 2017. Microvascular anomaly conditions in psychiatric disease. *Schizophrenia - angiogenesis connection*. *Neurosci. Biobehav. Rev.* 77, 327–339.
- Kawano, T., Ohmori, Y., Kaku, Y., Muta, D., Uekawa, K., Nakagawa, T., Amadatsu, T., Kasamo, D., Shiraishi, S., Kitajima, M., Kuratsu, J., 2016. Prolonged mean transit time detected by dynamic susceptibility contrast magnetic resonance imaging predicts cerebrovascular reserve impairment in patients with Moyamoya disease. *Cerebrovasc. Dis.* 42 (1–2), 131–138.
- Khalil, A.A., Ostwaldt, A.C., Nierhaus, T., Ganeshan, R., Audebert, H.J., Villringer, K., Villringer, A., Fiebach, J.B., 2017. Relationship between changes in the temporal dynamics of the blood-oxygen-level-dependent signal and hypoperfusion in acute ischemic stroke. *Stroke* 48 (4), 925–931.
- Kielar, A., Deschamps, T., Chu, R.K., Jokel, R., Khatamian, Y.B., Chen, J.J., Meltzer, J.A., 2016. Identifying dysfunctional cortex: dissociable effects of stroke and aging on resting state dynamics in MEG and fMRI. *Front. Aging Neurosci.* 8, 40.
- Kim, J.H., Taylor, A.J., Wang, D.J., Zou, X., Ress, D., 2019. Dynamics of the cerebral blood flow response to brief neural activity in human visual cortex. *J. Cerebr. Blood Flow Metabol.* Aug 20:271678X19869034. doi: 19869010.19861177/10271678X19869034.
- Kim, T., Kim, S.G., 2011. Temporal dynamics and spatial specificity of arterial and venous blood volume changes during visual stimulation: implication for BOLD quantification. *J. Cerebr. Blood Flow Metabol.* 31 (5), 1211–1222.
- Kong, Y., Zheng, Y., Johnston, D., Martindale, J., Jones, M., Billings, S., Mayhew, J., 2004. A model of the dynamic relationship between blood flow and volume changes during brain activation. *J. Cerebr. Blood Flow Metabol.* 24 (12), 1382–1392.
- Kwong, K.K., Belliveau, J.W., Chesler, D.A., Goldberg, I.E., Weisskoff, R.M., Poncelet, B.P., Kennedy, D.N., Hoppel, B.E., Cohen, M.S., Turner, R., et al., 1992. Dynamic magnetic resonance imaging of human brain activity during primary sensory stimulation. *Proc. Natl. Acad. Sci. U. S. A.* 89 (12), 5675–5679.
- Leroux, C., Bourourou, M., Hamel, E., 2019. How reliable is cerebral blood flow to map changes in neuronal activity? *Auton. Neurosci.* 217, 71–79.
- Leenders, K.L., Perani, D., Lammertsma, A.A., Heather, J.D., Buckingham, P., Healy, M.J., Gibbs, J.M., Wise, R.J., Hatazawa, J., Herold, S., et al., 1990. Cerebral blood flow, blood volume and oxygen utilization. Normal values and effect of age. *Brain* 113 (Pt 1), 27–47.
- Lewis, L.D., Setsompop, K., Rosen, B.R., Polimeni, J.R., 2016. Fast fMRI can detect oscillatory neural activity in humans. *Proc. Natl. Acad. Sci. U. S. A.* 113 (43), E6679–E6685.
- Liang, X., Zou, Q., He, Y., Yang, Y., 2013. Coupling of functional connectivity and regional cerebral blood flow reveals a physiological basis for network hubs of the human brain. *Proc. Natl. Acad. Sci. U. S. A.* 110 (5), 1929–1934.
- Lim, H.K., Nebes, R., Snitz, B., Cohen, A., Mathis, C., Price, J., Weissfeld, L., Klunk, W., Aizenstein, H.J., 2014. Regional amyloid burden and intrinsic connectivity networks in cognitively normal elderly subjects. *Brain* 137 (Pt 12), 3327–3338.
- Liu, E.Y., Haist, F., Dubowitz, D.J., Buxton, R.B., 2019. Cerebral blood volume changes during the BOLD post-stimulus undershoot measured with a combined normoxia/hyperoxia method. *Neuroimage* 185, 154–163.
- Liu, P., Pinho, M., Li, Y., Pan, L., Welch, B., Lu, H., 2017. Towards self-calibrated functional connectivity mapping. *Proc. Int'l. Soc. Mag. Reson. Med.* 25, 1665.
- Liu, T.T., 2013. Neurovascular factors in resting-state functional MRI. *Neuroimage* 80, 339–348.
- Li, W., van Zijl, P.C.M., 2020. Quantitative theory for the transverse relaxation time of blood water. *NMR Biomed.* Feb 5, e4207. <https://doi.org/10.1002/nbm.4207> [Epub ahead of print].
- Lu, H., Xu, F., Grgac, K., Liu, P., Qin, Q., van Zijl, P., 2012. Calibration and validation of TRUST MRI for the estimation of cerebral blood oxygenation. *Magn. Reson. Med.* 67 (1), 42–49.
- Lv, Y., Margulies, D.S., Cameron Craddock, R., Long, X., Winter, B., Gierkink, D., Endres, M., Villringer, K., Fiebach, J., Villringer, A., 2013. Identifying the perfusion deficit in acute stroke with resting-state functional magnetic resonance imaging. *Ann. Neurol.* 73 (1), 136–140.
- Manoliu, A., Riedl, V., Zherdin, A., Muhlau, M., Schwerthoffer, D., Scherr, M., Peters, H., Zimmer, C., Forstl, H., Baum, J., Wohlschlager, A.M., Sorg, C., 2014. Aberrant dependence of default mode/central executive network interactions on anterior insular salience network activity in schizophrenia. *Schizophr. Bull.* 40 (2), 428–437.
- Mateo, C., Knutson, P.M., Tsai, P.S., Shih, A.Y., Kleinfeld, D., 2017. Entrainment of arteriole vasomotor fluctuations by neural activity is a basis of blood-oxygenation-level-dependent "Resting-State" connectivity. *Neuron* 96 (4), 936–948 e933.
- Matsui, T., Murakami, T., Ohki, K., 2016. Transient neuronal coactivations embedded in globally propagating waves underlie resting-state functional connectivity. *Proc. Natl. Acad. Sci. U. S. A.* 113 (23), 6556–6561.
- Mayer, A., Schwedrick, C.M., Wibrat, M., Singer, W., Melloni, L., 2016. Expecting to see a letter: alpha oscillations as carriers of top-down sensory predictions. *Cerebr. Cortex* 26 (7), 3146–3160.
- Melie-García, L., Sanabria-Díaz, G., Sánchez-Catasús, C., 2013. Studying the topological organization of the cerebral blood flow fluctuations in resting state. *Neuroimage* 64, 173–184.
- Merola, A., Murphy, K., Stone, A.J., Germuska, M.A., Griffeth, V.E.M., Blockley, N.P., Buxton, R.B., Wise, R.G., 2016. Measurement of oxygen extraction fraction (OEF): an optimized BOLD signal model for use with hypercapnic and hyperoxic calibration. *Neuroimage* 129, 159–174.
- Mitra, A., Kraft, A., Wright, P., Acland, B., Snyder, A.Z., Rosenthal, Z., Czerniewski, L., Bauer, A., Snyder, L., Culver, J., Lee, J.M., Raichle, M.E., 2018. Spontaneous infra-slow brain activity has unique spatiotemporal dynamics and laminar structure. *Neuron* 98 (2), 297–305 e296.
- Mullinger, K.J., Cherukara, M.T., Buxton, R.B., Francis, S.T., Mayhew, S.D., 2017. Post-stimulus fMRI and EEG responses: evidence for a neuronal origin hypothesized to be inhibitory. *Neuroimage* 157, 388–399.
- Obata, T., Liu, T.T., Miller, K.L., Luh, W.M., Wong, E.C., Frank, L.R., Buxton, R.B., 2004. Discrepancies between BOLD and flow dynamics in primary and supplementary motor areas: application of the balloon model to the interpretation of BOLD transients. *Neuroimage* 21 (1), 144–153.
- Ogawa, S., Menon, R.S., Tank, D.W., Kim, S.G., Merkle, H., Ellermann, J.M., Ugurbil, K., 1993. Functional brain mapping by blood oxygenation level-dependent contrast magnetic resonance imaging. A comparison of signal characteristics with a biophysical model. *Biophys. J.* 64 (3), 803–812.
- Ogawa, S., Tank, D.W., Menon, R., Ellermann, J.M., Kim, S.G., Merkle, H., Ugurbil, K., 1992. Intrinsic signal changes accompanying sensory stimulation: functional brain mapping with magnetic resonance imaging. *Proc. Natl. Acad. Sci. U. S. A.* 89 (13), 5951–5955.
- Oliveira, I.A.F., Guimarães, T.M., Souza, R.M., Dos Santos, A.C., Machado-de-Sousa, J.P., Hallak, J.E.C., Leoni, R.F., 2018. Brain functional and perfusional alterations in schizophrenia: an arterial spin labeling study. *Psychiatry Res. Neuroimaging*, 272, 71–78.

- Ostergaard, L., Aamand, R., Gutierrez-Jimenez, E., Ho, Y.C., Blicher, J.U., Madsen, S.M., Nagenthiranja, K., Dalby, R.B., Drasbek, K.R., Moller, A., Braendgaard, H., Mouridsen, K., Jespersen, S.N., Jensen, M.S., West, M.J., 2013. The capillary dysfunction hypothesis of Alzheimer's disease. *Neurobiol. Aging* 34 (4), 1018–1031.
- Peca, S., McCreary, C.R., Donaldson, E., Kumarpillai, G., Shobha, N., Sanchez, K., Charlton, A., Steinback, C.D., Beaudin, A.E., Fluck, D., Pillay, N., Fick, G.H., Poulin, M.J., Frayne, R., Goodyear, B.G., Smith, E.E., 2013. Neurovascular decoupling is associated with severity of cerebral amyloid angiopathy. *Neurology* 81 (19), 1659–1665.
- Pelizzari, L., Lagana, M.M., Rossetto, F., Bergstrand, N., Galli, M., Baselli, G., Clerici, M., Nemni, R., Baglio, F., 2019. Cerebral blood flow and cerebrovascular reactivity correlate with severity of motor symptoms in Parkinson's disease. *Ther Adv Neurol Disord* 12, 1756286419838354.
- Preibisch, C., Castrillon, G.J., Buhrer, M., Riedl, V., 2015. Evaluation of multiband EPI acquisitions for resting state fMRI. *PLoS One* 10 (9), e0136961.
- Preibisch, C., Sorg, C., Forschler, A., Grimmer, T., Sax, I., Wohlschlager, A.M., Pernecke, R., Forstl, H., Kurz, A., Zimmer, C., Alexopoulos, P., 2011. Age-related cerebral perfusion changes in the parietal and temporal lobes measured by pulsed arterial spin labeling. *J. Magn. Reson. Imag.* 34 (6), 1295–1302.
- Qin, Q., Grgac, K., van Zijl, P.C., 2011. Determination of whole-brain oxygen extraction fractions by fast measurement of blood T(2) in the jugular vein. *Magn. Reson. Med.* 65 (2), 471–479.
- Rangaprakash, D., Wu, G.R., Marinazzo, D., Hu, X., Deshpande, G., 2018. Hemodynamic response function (HRF) variability confounds resting-state fMRI functional connectivity. *Magn. Reson. Med.* 80 (4), 1697–1713.
- Richter, V., Helle, M., van Osch, M.J.P., Lindner, T., Gersing, A.S., Tsantilas, P., Eckstein, H.H., Preibisch, C., Zimmer, C., 2017. MR imaging of individual perfusion reorganization using superselective pseudocontinuous arterial spin-labeling in patients with complex extracranial steno-occlusive disease. *Am. J. Neuroradiol.* 38 (4), 703–711.
- Riederer, I., Bohn, K.P., Preibisch, C., Wiedemann, E., Zimmer, C., Alexopoulos, P., Forster, S., 2018. Alzheimer disease and mild cognitive impairment: integrated pulsed arterial spin-labeling MRI and F-18-FDG PET. *Radiology* 288 (1), 198–206.
- Ritter, P., Schirmer, M., McIntosh, A.R., Jirsa, V.K., 2013. The virtual brain integrates computational modeling and multimodal neuroimaging. *Brain Connect.* 3 (2), 121–145.
- Ruiz-Rizzo, A.L., Beissner, F., Finke, K., Müller, H.J., Zimmer, C., Pasquini, L., Sorg, C., 2020. Human subsystems of medial temporal lobes extend locally to amygdala nuclei and globally to an allostatic-interoceptive system. *Neuroimage* 207, 116404.
- Sanchez-Vives, M.V., Mattia, M., 2014. Slow wave activity as the default mode of the cerebral cortex. *Arch. Ital. Biol.* 152 (2–3), 147–155.
- Sanz-Leon, P., Knock, S.A., Spiegler, A., Jirsa, V.K., 2015. Mathematical framework for large-scale brain network modeling in the Virtual Brain. *Neuroimage* 111, 385–430.
- Schirmer, M., McIntosh, A.R., Jirsa, V., Deco, G., Ritter, P., 2018. Inferring multi-scale neural mechanisms with brain network modelling. *Elife* 7.
- Schoffelen, J.M., Oostenveld, R., Fries, P., 2005. Neuronal coherence as a mechanism of effective corticospinal interaction. *Science* 308 (5718), 111–113.
- Setsopop, K., Feinberg, D.A., Polimeni, J.R., 2016. Rapid brain MRI acquisition techniques at ultra-high fields. *NMR Biomed.* 29 (9), 1198–1221.
- Simon, A.B., Buxton, R.B., 2015. Understanding the dynamic relationship between cerebral blood flow and the BOLD signal: implications for quantitative functional MRI. *Neuroimage* 116, 158–167.
- Sorg, C., Riedl, V., Muhlau, M., Calhoun, V.D., Eichele, T., Laer, L., Drzezga, A., Forstl, H., Kurz, A., Zimmer, C., Wohlschlager, A.M., 2007. Selective changes of resting-state networks in individuals at risk for Alzheimer's disease. *Proc. Natl. Acad. Sci. U. S. A.* 104 (47), 18760–18765.
- Stickland, R., Allen, M., Magazzini, L., Singh, K.D., Wise, R.G., Tomassini, V., 2019. Neurovascular coupling during visual stimulation in multiple sclerosis: a MEG-fMRI study. *Neuroscience* 403, 54–69.
- Stone, A.J., Blockley, N.P., 2017. A streamlined acquisition for mapping baseline brain oxygenation using quantitative BOLD. *Neuroimage* 147, 79–88.
- Tak, S., Polimeni, J.R., Wang, D.J., Yan, L., Chen, J.J., 2015. Associations of resting-state fMRI functional connectivity with flow-BOLD coupling and regional vasculature. *Brain Connect.* 5 (3), 137–146.
- Tak, S., Wang, D.J., Polimeni, J.R., Yan, L., Chen, J.J., 2014. Dynamic and static contributions of the cerebrovasculature to the resting-state BOLD signal. *Neuroimage* 84, 672–680.
- Triantafyllou, C., Polimeni, J.R., Wald, L.L., 2011. Physiological noise and signal-to-noise ratio in fMRI with multi-channel array coils. *Neuroimage* 55 (2), 597–606.
- Wesolowski, R., Blockley, N.P., Driver, I.D., Francis, S.T., Gowland, P.A., 2019. Coupling between cerebral blood flow and cerebral blood volume: contributions of different vascular compartments. *NMR Biomed.* 32 (3), e4061.
- West, K.L., Zuppichini, M.D., Turner, M.P., Sivakolundu, D.K., Zhao, Y., Abdelkarim, D., Spence, J.S., Rypma, B., 2019. BOLD hemodynamic response function changes significantly with healthy aging. *Neuroimage* 188, 198–207.
- Whittaker, J.R., Driver, I.D., Venzi, M., Bright, M.G., Murphy, K., 2019. Cerebral autoregulation evidenced by synchronized low frequency oscillations in blood pressure and resting-state fMRI. *Front. Neurosci.* 13, 433.
- Wise, R.G., Harris, A.D., Stone, A.J., Murphy, K., 2013. Measurement of OEF and absolute CMRO₂: MRI-based methods using interleaved and combined hypercapnia and hyperoxia. *Neuroimage* 83, 135–147.
- Wu, G.R., Di Perri, C., Charland-Verville, V., Martial, C., Carriere, M., Vanhaudenhuyse, A., Laureys, S., Marinazzo, D., 2019. Modulation of the spontaneous hemodynamic response function across levels of consciousness. *Neuroimage* 200, 450–459.
- Wu, G.R., Liao, W., Stramaglia, S., Ding, J.R., Chen, H., Marinazzo, D., 2013. A blind deconvolution approach to recover effective connectivity brain networks from resting state fMRI data. *Med. Image Anal.* 17 (3), 365–374.
- Yablonskiy, D.A., 1998. Quantitation of intrinsic magnetic susceptibility-related effects in a tissue matrix. Phantom study. *Magn. Reson. Med.* 39 (3), 417–428.
- Yablonskiy, D.A., Haacke, E.M., 1994. Theory of NMR signal behavior in magnetically inhomogeneous tissues: the static dephasing regime. *Magn. Reson. Med.* 32 (6), 749–763.
- Zalesky, A., Fornito, A., Cocchi, L., Gollop, L.L., Breakspear, M., 2014. Time-resolved resting-state brain networks. *Proc. Natl. Acad. Sci. U. S. A.* 111 (28), 10341–10346.
- Zhang, D., Raichle, M.E., 2010. Disease and the brain's dark energy. *Nat. Rev. Neurol.* 6 (1), 15–28.
- Zhou, J., Greicius, M.D., Gennatas, E.D., Growdon, M.E., Jang, J.Y., Rabinovici, G.D., Kramer, J.H., Weiner, M., Miller, B.L., Seeley, W.W., 2010. Divergent network connectivity changes in behavioural variant frontotemporal dementia and Alzheimer's disease. *Brain* 133 (Pt 5), 1352–1367.
- Zhu, D.C., Tarumi, T., Khan, M.A., Zhang, R., 2015. Vascular coupling in resting-state fMRI: evidence from multiple modalities. *J. Cerebr. Blood Flow Metabol.* 35 (12), 1910–1920.